RSS Models for Respiration Rate Monitoring

Hüseyin Yiğitler, Ossi Kaltiokallio, Roland Hostettler,
Alemayehu Solomon Abrar, Riku Jäntti, Neal Patwari, and Simo Särkkä

This is a pre-print of a paper accepted for publication in *IEEE Transactions on Mobile Computing*. When citing this work, you must always cite the original article:

> H. Yiğitler, O. Kaltiokallio, R. Hostettler, A. S. Abrar, R. Jäntti, N. Patwari, and S. Särkkä, "RSS models for respiration rate monitoring," *IEEE Transactions on Mobile Computing*, 2019, to appear

DOI:

10.1109/TMC.2019.2897682

RSS Models for Respiration Rate Monitoring

Hüseyin Yiğitler, Ossi Kaltiokallio, Roland Hostettler, Alemayehu Solomon Abrar
Riku Jäntti, Neal Patwari and Simo Särkkä

Abstract—Received signal strength based respiration rate monitoring is emerging as an alternative non-contact technology. These systems make use of the radio measurements of short-range commodity wireless devices, which vary due to the inhalation and exhalation motion of a person. The success of respiration rate estimation using such measurements depends on the signal-to-noise ratio, which alters with properties of the person and with the measurement system. To date, no model has been presented that allows evaluation of different deployments or system configurations for successful breathing rate estimation. In this paper, a received signal strength model for respiration rate monitoring is introduced. It is shown that measurements in linear and logarithmic scale have the same functional form, and the same estimation techniques can be used in both cases. The model is numerically and empirically evaluated, and its properties are discussed in depth. The most important model implications are validated under varying signal-to-noise ratio conditions using the performances of three estimators: batch frequency estimator, recursive Bayesian estimator, and model-based estimator. The results are in coherence with the findings, and they imply that different estimators are advantageous in different signal-to-noise ratio regimes.

Index Terms—radio frequency propagation, received signal strength measurements, respiration rate monitoring, frequency estimation

1 Introduction

Respiratory rate is an important vital sign that can be used to monitor the progression of an illness [1], and to predict events that need immediate clinical attention such as a cardiac arrest [2]. The importance of this vital sign is well acknowledged, and both contact and non-contact measurement systems are commercially available [3]. Non-contact respiration rate monitoring is advantageous compared to contact systems in terms of improved patient's comfort and less patient distress, which result in improved accuracy. In this paper, we consider non-contact respiration rate monitoring using the received signal measurements of commercially available low-cost standard wireless nodes. The main aim of these kind of systems is to estimate the respiration rate using the low-amplitude signal variations due to inhale and exhale motion.

The impact of respiration on the received signal has a complex relationship with the geometry and electrical properties of the objects in the environment, which is referred to as the *radio channel*. As the granularity of the channel measurements increases, the information about the respiration can be better seen in the measurements. For example, high granularity measurements of different radar systems can be used for developing high quality monitoring systems [4]–[6]. However, higher quality channel measurements require complicated and expensive measurement systems. In contrast, monitoring systems based on commercially available narrowband communication systems are readily available, cheap, and easy to deploy. For example, several studies have evaluated the performance and different aspects of orthogonal-frequency-division-multiplexing (OFDM) based WiFi (IEEE 802.11 a, g, n, ac) [7], and low-power IEEE 802.15.4 compliant [8]–[10] systems. In this paper, narrowband and low-power systems, which provide received signal strength (RSS) measurements to assess the state of the propagation channel, are considered. Such measurements are the most challenging for breathing monitoring since their measurements provide only coarse information about the channel. However, it is possible to build very low-cost systems using off-the-shelf components or using already available radios of mobile devices or smart appliances.

Breathing monitoring using narrowband systems can be efficiently realized using a single pair of transmitter (TX) and receiver (RX) nodes [8]. The RSS measurements of the RX can be modeled as a single tone sinusoid contaminated with noise [9], which is given by

$$\zeta(t_k) = a_0 + a_1 \cos(2\pi f t_k + \Phi) + n_z(t_k), \tag{1}$$

where a_0 is the DC shift[1], a_1 is the amplitude of the sinusoidal signal, f is the respiration rate, Φ is the phase offset of the breathing, t_k is the k^{th} sample time, and $n_z(t_k)$ is the measurement noise. The maximum likelihood estimate of f using the discrete time observations $\zeta(t_k)$ is known to be equivalent to the peak of the discrete power spectral density of the measurements [11]. However, the estimation quality of this estimator exhibits a thresholding behavior depending on the signal-to-noise ratio (SNR) of the measurements, which is mainly defined by the model parameter

Hüseyin Yiğitler, Ossi Kaltiokallio, and Riku Jäntti are with Aalto University, Department of Communications and Networking. e-mail: {name.surname}@aalto.fi
Roland Hostettler and Simo Särkkä are with Aalto University, Department of Electrical Engineering and Automation. e-mail: {name.surname}@aalto.fi
Alemayehu Solomon Abrar is with the Dept. of Electrical & Computer Engineering, University of Utah, Salt Lake City, UT 84112 USA (e-mail: aleksol.abrar@utah.edu).
Neal Patwari is with the Dept. of Electrical & Computer Engineering, University of Utah, and Xandem Technology LLC, Salt Lake City, UT 84112 USA (e-mail: npatwari@ece.utah.edu).

1. This term is usually eliminated by band-pass filtering or by DC removal, and not considered as a model parameter.

a_1, and the variance of the noise $n_z(t_k)$. When the SNR is low, the mean-square-error increases very rapidly and the estimation performance quickly degrades. This estimator is used by the previous works without forming an explicit link between physical parameters[2] and the model parameter a_1, which is required to investigate the underlying reasons of performance degradation of respiration rate estimation. The work in this paper fills this gap by introducing an RSS model in terms of physical parameters for respiration rate monitoring. The model allows one to predict the expected performance for a deployment scenario and patient's position, and better assess the required system configuration for successful breathing monitoring.

In this paper, an RSS model of narrowband communication systems for respiration rate monitoring is presented. The model is derived for the respiration rate monitoring starting from the reflection based RSS model, which was previously explored for RSS-based localization [14], [15]. Based on this model, first, it is shown that the breathing signal is frequency modulated into the RSS in linear scale due to small periodic movements. Such a signal exhibits relatively strong components on more than one frequency tone so that breathing estimators making use of this feature (see [16]) perform better in high SNR conditions. Then, it is shown that the RSS in logarithmic scale also has the same form, and an explicit model is derived. The model itself allows us to evaluate feasibility of different breathing rate estimation techniques by enabling SNR evaluation of any given deployment. The impact of several parameters are evaluated both numerically and empirically. This paper makes the following contributions:

- A series expansion of the reflection-based RSS model is derived. This allows one to find several approximations to the observed RSS variations.
- An RSS model for small periodic perturbations (e.g. breathing motion) is derived. It is shown that the RSS variation due to such a motion yields discrete tones at the harmonics of the perturbation frequency. In particular, a single tone approximation of the model allows one to represent the model model parameter a_1 in Eq. (1) as a function of physical parameters. This allows explicit SNR calculation for a given deployment and patient's position, geometry and electromagnetic properties.
- It is also shown that when the object has a non-zero velocity, the movement shifts the frequency of the periodic movement, making the estimation a challenging problem.
- Based on the models, various scenarios observed in empirical data are discussed and their impact on the observed RSS is shown.
- Three different respiration rate estimators are compared, and their performances are linked to the implications of the model.

The remaining part of the paper is organized as follows. First, the related work is summarized in Section 2. The RSS measurement model and its series expansion are derived in Section 3. The model implications are discussed after numerical evaluation and empirical validation in Section 4. The breathing rate estimation techniques are introduced in Section 5, before giving empirical evaluations in Section 6. The conclusions are drawn in Section 7.

2. Electromagnetic constitutional parameters (electrical permittivity, magnetic permeability and conductivity) of a considered propagation scenario and the geometrical parameters of a TX-RX pair and the surroundings (including the objects of interest) are referred to as physical parameters. Interested reader is referred to [12] and [13, ch. 3] for a detailed description of the physical parameters.

2 Related Work

The importance of respiration rate has resulted in development of several respiration rate monitoring systems using different physical parameters (e.g. temperature, chest effort) [3]. In this section, we only provide a brief review of radio-frequency based respiration rate monitoring methods, focusing on RSS-based approaches. The reader is referred to, for example, the works by AL-Khalidi et al. [3] and Folke et al. [17] for comprehensive technological overviews.

Respiration rate monitoring using radio frequency devices is a non-contact solution that has attracted significant attention. There are three different radar technologies that have been used for the purpose as has been reviewed by Li et al. [18]. The first work that appeared in the literature uses continuous wave (CW) Doppler radar system. Several studies have been published to analyze different aspect of these systems, and it has been shown that they can estimate the heart rate along with the respiration rate [19]. The impulse radio ultra wideband (IR-UWB) systems are also used for respiration rate monitoring [5]. They radiate and consume little power, may coexist well with other instruments, and perform better in environments with interference and severe multipath [20]. The characteristics of the received signal of IR-UWB systems were investigated by Venkatesh et al. [21]. However, these systems cannot cope with the impact of other motion or presence of more than one person [6]. Linear frequency modulated continuous wave (LFM-CW) systems can distinguish different reflector positions using their linearly varying frequency. This property has been used by Adib et al. for first estimating position of multiple persons in an environment [22], and then estimating the vital signs of each individual [6]. In this work, we show that indeed RSS has similar characteristics as the measurements of radar solutions, but require more carefully adjusted deployments.

The radar based solutions require a sophisticated hardware development for the vital sign monitoring. However, recent works on environmental sensing motivated RSS-based respiration rate monitoring using commodity wireless communication devices. The first work studying the feasibility of such systems makes use of multiple links formed by a mesh network of IEEE 802.15.4 nodes to estimate the breathing rate of a single person in the environment [9]. Later, this system was extended to estimate the location of a breathing person [10]. Several practical problems associated with the system are addressed in [8] by using only one pair of TX-RX nodes, detecting the moments breathing estimation is not possible, and using various signal processing techniques to improve SNR of the measurements. Due to widespread availability of WiFi, the communication channel measurements of these systems have also been used for respiration monitoring [7], [23]. The work by Abdelnasser et al. is based on the RSS measurements of WiFi systems [23]. On the other hand, the channel state information (CSI) output of OFDM-based WiFi radios provide higher granularity measurements

of the communication channel, and have been used for vital sign monitoring purposes [24]–[26]. The CSI contains a complex channel gain estimate[3] at each sub-carrier. In case the transmitted power is constant, the amplitude variation of these gains define the RSS variation at each sub-carrier in the linear scale. It can be argued that the RSS-based models and algorithms can be applied directly to CSI-based systems that use amplitudes of the complex CSI vector components. Therefore, RSSI based system developments are more general, and provides insights on the worst case performance of CSI based developments.

In this work, we model the RSS of narrowband communication systems for small periodic perturbations with unknown frequency, direction, and amplitude. It is shown that, similar to the signals in the radar systems developed by Venkatesh et al. [21], the received RF signal contains the frequency modulated periodic vital signals, which has a periodic series representation. The resulting model shows explicit relation between the respiration signal and initial position of the person, their orientation with respect to the link-line, their electrical properties, the amplitude of the breathing, and the wavelength of the communication system. Due to the logarithmic transformation taking place in typical RSS measurement systems [27], we also show that the RSS measurements in a logarithmic scale has a series representation having non-zero tones at only the discrete multiples of the respiration rate. These results show that the single tone model in Eq. (1) is an approximation to both linear scale and logarithmic scale RSS measurements. The series coefficients allow one to calculate the SNR of the respiration signal, which in turn enables assessing the performance of single tone parameter estimation techniques [11]. Therefore, this work covers the derivations for IR-UWB radars [21], extends them for practical RSS measurement systems, and represents the model parameters as functions of physical parameters.

The respiration rate monitoring using the radio channel measurements have the similar characteristics among different technologies as recently been studied by Hillyard et al. [28]. In the work, four different technologies are compared, and it is identified that approximately half of the estimates are within 1 breaths-per-minute neighborhood of the actual respiration rate. As the derived models in this work imply, regardless of the technology, this performance is as expected since the SNR of the measurements is mainly defined by the person's orientation with respect to link-line and their position. Similarly, the derived model is coherent with empirical results of Luong et al. [29], real-time spectrum analyzer measurements in [8], and findings of Wang et al. [25]. The model describes the implications of these empirical works, while also shedding light on various interesting situations arising in practical deployments; e.g., the measurements showing only odd or even harmonics depending on the physical parameters. In summary, the developed model can be used for validating and planning various deployment conditions that enable successful breathing rate monitoring.

3. CSI is available in OFDM based WiFi devices, and it is a vendor specific channel measurement output such that its dependence on the communication channel parameters may be different for different brands. However, in principle, they all can be converted to RSS measurements. On the other hand, RSSI is ubiquitously available in wireless nodes, including the ones of low-cost wireless communication technologies (e.g. Bluetooth).

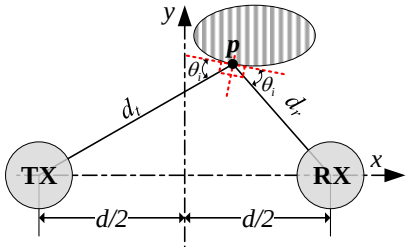

Fig. 1. A propagation scenario for RSS modeling and considered reference frame. The transmitter (TX) node placed on point $\boldsymbol{p}_t$ emits a narrowband signal and the receiver (RX) node placed on $\boldsymbol{p}_r$ receives the signal. Incident ray is reflected from point $\boldsymbol{p}$ on the surface of the object, which has a distance $d_t = \|\boldsymbol{p}_t - \boldsymbol{p}\|$ m to the TX and $d_r = \|\boldsymbol{p}_r - \boldsymbol{p}\|$ m to the RX. The incident ray has θ_i radians incidence angle. The TX and RX are separated by $d = \|\boldsymbol{p}_t - \boldsymbol{p}_r\|$ m.

3 Received Signal Strength Models

In this section, we first review the RSS model, and then derive temporal variations of the RSS in linear scale for an object[4] making movements in the form

$$\boldsymbol{p}(t) = \boldsymbol{p}_0 + g(t)\boldsymbol{\delta}, \tag{2}$$

where $\boldsymbol{p}_0$ is a reference point at $t = 0$, t is the time elapsed since the epoch, $g(t)$ is the low-amplitude periodic displacement with frequency f and $\|\boldsymbol{\delta}\| = 1$ is the constant movement direction for the Euclidean norm $\|\cdot\|$. Then, the derived models are extended for the RSS measurement systems that perform logarithmic transformations.

3.1 Background

For environmental sensing applications, the phenomenon of interest is estimated using the variation in RSS measurements $\mathcal{P}[k]$ compared to the measurement acquired when the object of interest is not in the medium, that is, the baseline RSS $\mathcal{P}_r$. A detailed analysis of the baseline RSS is provided in [27], and it is concluded that if the complex channel gain α is constant, RSS is approximately a Gaussian random variable. This result also implies that if the medium is constant for the duration of acquiring the baseline RSS, their population mean converges to a constant $\mathcal{P}_r$ due to the *strong law of large numbers* (SLLN). Then, the time average of the measurements also converges to the same constant since the channel is mean ergodic when the environment is static. In other words, the baseline RSS $\mathcal{P}_r$ is given by

$$\mathcal{P}_r = 10\log_{10}(2\sigma^2 + \varrho\sigma^2), \tag{3}$$

where ϱ is the signal-to-noise ratio (SNR) of the received signal under static channel conditions, and σ^2 is the noise variance of the zero mean Gaussian noise in signal samples.

4. In this paper, we assume that the object is rigid so that any movement affects all points in its interior and on its boundary by the same amount.

Therefore, a practical measurement model[5] for environmental sensing applications is

$$r[k] \triangleq \mathcal{P}[k] - \mathcal{P}_r \approx 10\log_{10}\left(\frac{|\alpha[k]|^2}{|\alpha_r|^2}\right) + \nu[k], \quad (4)$$

where $\alpha[k]$ is the channel gain when k^{th} RSS sample is acquired, and α_r is the constant channel gain of the baseline RSS. The last term $\nu[k]$ is the joint noise process of all noise sources including white noise, round-off errors, quantization noise, and any source of uncertainty due to modeling errors, and its variance depends also on the current SNR value $\varrho[k]$, which is time varying for the non-static case.

The expression in Eq. (4) implies that the complex channel gains $\alpha[k]$ and α_r define the measurements. For the scenario visualized in Fig. 1, the ratio of the channel gains[6] has already been investigated in [14] and [15]. It has been shown that the ratio can be written as

$$R \triangleq \frac{|\alpha|^2}{|\alpha_r|^2} = 1 + G^2 - 2G\cos\left(\frac{2\pi\Delta}{\lambda}\right), \quad (5)$$

where Δ is excess path length traversed by the ray reflected from the object's surface compared to the direct path, G is the *effective reflection coefficient*, λ denotes the wavelength, and we have dropped sample index $[k]$ from G and Δ. The effective reflection coefficient is defined as

$$G \triangleq \frac{\Gamma}{(1+\Delta/d)^{\eta/2}}, \quad (6)$$

where Γ is the Fresnel reflection coefficient and η is the path loss exponent modeling the fading experienced by both of the components [30, ch. 4]. The excess path length Δ parametrizes the ellipse tangent to the interacting object at the point $\boldsymbol{p}$ (cf. Fig. 1), and is defined as

$$\Delta \triangleq \|\boldsymbol{p} - \boldsymbol{p}_t\| + \|\boldsymbol{p} - \boldsymbol{p}_r\| - \|\boldsymbol{p}_r - \boldsymbol{p}_t\| = d_t + d_r - d, \quad (7)$$

for the symbols visualized on Fig. 1.

3.2 Effect of Low-amplitude Periodic Perturbations

In the previous section, we analyzed the variation of RSS when the object abruptly appears in position which yield Δ meters of excess path length when $\boldsymbol{p}_0$ is the reflection point shown in Fig. 1. Now, suppose the object makes a time varying movement in a constant direction $\boldsymbol{\delta}$, that is, the reflection point $\boldsymbol{p}_0$ moves to $\boldsymbol{p}(t) = \boldsymbol{p}_0 + g(t)\boldsymbol{\delta}$ at time instant t. At this new position, the excess path length can be found using its Taylor series expansion around $\boldsymbol{p} = \boldsymbol{p}_0$ as

$$\Delta(\boldsymbol{p}) = \Delta(\boldsymbol{p}_0) + g(t)(\nabla_{\boldsymbol{p}}\Delta)^\top\boldsymbol{\delta} + \mathcal{O}(g^2(t)),$$

where superscript $^\top$ denotes the matrix transpose, $\nabla_{\boldsymbol{p}}$ is the gradient with respect to position $\boldsymbol{p}$, and we have used the fact that Δ is a smooth function of both coordinates except at $\boldsymbol{p} = \boldsymbol{p}_r$ or $\boldsymbol{p} = \boldsymbol{p}_t$. If the movement has a small amplitude $|g(t)| \ll 1$, the second and higher order terms in the Taylor series expansion can be ignored, and one can write

$$\Delta(\boldsymbol{p}) \approx \Delta_0 + g(t)\left[\frac{\boldsymbol{p}_0 - \boldsymbol{p}_r}{\|\boldsymbol{p}_0 - \boldsymbol{p}_r\|} + \frac{\boldsymbol{p}_0 - \boldsymbol{p}_t}{\|\boldsymbol{p}_0 - \boldsymbol{p}_t\|}\right]^\top\boldsymbol{\delta}, \quad (8)$$

where $\Delta_0 = \Delta(\boldsymbol{p}_0)$ and we have explicitly written the gradient of Δ with respect to $\boldsymbol{p}$ at $\boldsymbol{p} = \boldsymbol{p}_0$. Let us denote the inner product in Eq. (8) as

$$\delta_\Delta \triangleq \left[\frac{\boldsymbol{p}_0 - \boldsymbol{p}_r}{\|\boldsymbol{p}_0 - \boldsymbol{p}_r\|} + \frac{\boldsymbol{p}_0 - \boldsymbol{p}_t}{\|\boldsymbol{p}_0 - \boldsymbol{p}_t\|}\right]^\top\boldsymbol{\delta}. \quad (9)$$

Then, Eq. (5) can be written as

$$R \approx 1 + G^2(\boldsymbol{p}) - 2G(\boldsymbol{p})\cos\left(2\pi\frac{\delta_\Delta}{\lambda}g(t) + 2\pi\frac{\Delta_0}{\lambda}\right). \quad (10)$$

It is to be noted that, for small amplitude perturbations satisfying $|g(t)\delta_\Delta| \ll d$, we have $G(\boldsymbol{p}) \approx G(\boldsymbol{p}_0)$. Consequently, the frequency of the cosine term in Eq. (10) is defined by the perturbation amplitude $g(t)\delta_\Delta$, i.e., R is a frequency modulated version of $g(t)$.

The amplitude ratio R can be further simplified when $g(t)$ is a periodic function[7]. Suppose that $g(t) = A\sin(2\pi ft)$, so that the *affective amplitude of the periodic movement* A, and constant phase ψ can be defined as

$$\tilde{A} \triangleq 2\pi A\frac{\delta_\Delta}{\lambda}, \qquad \psi \triangleq 2\pi\frac{\Delta_0}{\lambda}. \quad (11)$$

Then, the Fourier series expansion of the cosine terms in Eq. (10) are given by

$$\cos\left(\tilde{A}\sin(2\pi ft) + \psi\right) = \sum_{m=-\infty}^{\infty} J_m(\tilde{A})\cos(2\pi mft + \psi),$$

where $J_m(\cdot)$ is the Bessel function of the first kind [32, ch. 9]. Substituting this into Eq. (10) yields

$$R_1 \approx 1 + G^2 - 2G\sum_{m=-\infty}^{\infty} J_m(\tilde{A})\cos(2\pi mft + \psi), \quad (12)$$

where we have dropped explicit dependence of $G(\boldsymbol{p}_0) \equiv G$. The expression in Eq. (12) has the form of demodulated and low-pass filtered version of the respiration signal of IR-UWB systems derived by Venkatesh et al. [21].

Using the properties of Bessel function, the expression in Eq. (12) can be written in the form

$$R_1 \approx c_0 + \sum_{m=1}^{\infty}\Big\{c_{2m-1}\sin(2\pi(2m-1)ft) + c_{2m}\cos(2\pi 2mft)\Big\}, \quad (13)$$

where the coefficients are given by

$$c_m = \begin{cases} 1 + G^2 - 2GJ_0(\tilde{A})\cos(\psi), & m = 0, \\ 4GJ_m(\tilde{A})\sin(\psi), & m \text{ is odd}, \\ -4GJ_m(\tilde{A})\cos(\psi), & m \text{ is even}. \end{cases} \quad (14)$$

5. A detailed derivation of the model can be found in [12], and the underlying model assumptions are discussed in [14]. In the remaining part of this paper, we assume that the model assumptions are satisfied.

6. The channel gain ratio follows from logarithmic scale definitions. If linear scale measurements are going to be used without calculating the amplitude ratio, the subsequent developments are valid through the relation $d^{-\eta/2}(R-1)$, which has the same spectral properties as R but with different DC term and amplitude scale. See Eq. (13) and its coefficients in Eq. (14).

7. The form of $g(t)$ is selected for simplicity. The analysis can be straightforwardly extended to any periodic function using their Fourier series expansion as it is shown in [31, ch. 5].

3.3 RSS in Logarithmic Scale

Let us define the amplitude ratio R in Eq. (5) in logarithmic scale as

$$\begin{aligned}\mathcal{R} \triangleq & 10\log_{10}(e)\ln(R) \\ = & \ 10\log_{10}(e)\ln\left(1+G^2\right) \\ & + 10\log_{10}(e)\ln\left(1-\kappa\cos\left(2\pi\beta\Delta\right)\right),\end{aligned} \tag{15}$$

where e is the base of the natural logarithm and we have defined

$$\beta \triangleq \frac{1}{\lambda}, \qquad \kappa \triangleq 2\frac{G}{1+G^2}. \tag{16}$$

It can easily be verified that $G < 1$ for $\Gamma < 1$ so that $0 < \kappa < 1$ and the power series expansion of the second term in Eq. (16) is given by

$$\begin{aligned}\ln\Big(1-\kappa\cos(2\pi\beta\Delta)\Big) &= -\sum_{l=1}^{\infty}\frac{1}{l}\big(\kappa\cos(2\pi\beta\Delta)\big)^l \\ &= b_0 + \sum_{i=1}^{\infty} b_i\cos(2\pi i\Delta\beta),\end{aligned}$$

where the coefficients are given by

$$b_i = -\Delta\int_{-\frac{1}{2\Delta}}^{\frac{1}{2\Delta}}\sum_{l=1}^{\infty}\frac{\kappa^l}{l}\cos^l(2\pi\Delta\beta)\cos(2\pi i\Delta\beta)d\beta,$$

for all $i \in \{0,1,2,\dots\}$. In addition, the cosine powers can be expanded as harmonics,

$$\cos^l(\theta) = \begin{cases}\frac{2}{2^l}\sum\limits_{i=0}^{\frac{l-1}{2}}\binom{l}{i}\cos\big((l-2i)\theta\big), & l \text{ odd},\\ \frac{1}{2^l}\binom{l}{\frac{l}{2}} + \frac{2}{2^l}\sum\limits_{i=0}^{\frac{l-2}{2}}\binom{l}{i}\cos\big((l-2i)\theta\big), & l \text{ even},\end{cases}$$

where θ is an arbitrary argument of $\cos(\cdot)$. Due to orthogonality of the sinusoidal functions, b_i are polynomials of κ which can be written as

$$b_i = \begin{cases}-\sum\limits_{l=1}^{\infty}\frac{\kappa^{2l}}{2l2^{2l}}\binom{2l}{l}, & i=0,\\ -\sum\limits_{l=\frac{i+1}{2}}^{\infty}\frac{2\kappa^{2l-1}}{(2l-1)2^{2l-1}}\binom{2l-1}{\frac{2l-i-1}{2}}, & i \text{ odd},\\ -\sum\limits_{l=\frac{i}{2}}^{\infty}\frac{2\kappa^{2l}}{(2l)2^{2l}}\binom{2l}{\frac{2l-i}{2}}, & i \text{ even}.\end{cases}$$

Note that $b_i < 0$ for all $i = 0,1,2,\cdots$, and for $\kappa < 1$ and $i > 0$ we have $|b_i| > |b_{i+1}|$. The partial sums of the coefficients are convergent, and after simplification and substituting definition of κ in Eq. (16) into this result yields

$$b_i = \begin{cases}-\ln\left(1+G^2\right), & i=0,\\ -2\frac{G^i}{i}, & i>0.\end{cases}$$

One important consequence is that b_0 is equal to the additive inverse of the first term in Eq. (15), and they cancel out. Therefore, the RSS measurement model in Eq. (15) can be written as

$$\mathcal{R} = -20\log_{10}(e)\sum_{i=1}^{\infty}\frac{G^i}{i}\cos\left(2\pi\frac{i}{\lambda}\Delta\right). \tag{17}$$

The series in Eq. (17) implies that the periodic sinusoidal perturbation in Eq. (12) after logarithmic transformation reads as

$$\begin{aligned}\mathcal{R}_1 \approx -20\log_{10}(e)\sum_{m=-\infty}^{\infty}\sum_{i=1}^{\infty}\Bigg\{&J_m(i\tilde{A})\frac{G^i}{i} \\ &\cos(2\pi mft + i\psi)\Bigg\},\end{aligned} \tag{18}$$

where $\psi = 2\pi\Delta(\boldsymbol{p}_0)/\lambda$. The series in Eq. (18) can be written in the form of Eq. (13),

$$\begin{aligned}\mathcal{R}_1 \approx \mathcal{c}_0 + \sum_{m=1}^{\infty}\Big\{&\mathcal{c}_{2m-1}\sin(2\pi(2m-1)ft) \\ &+ \mathcal{c}_{2m}\cos(2\pi 2mft)\Big\},\end{aligned} \tag{19}$$

where, for this case, the coefficients are given by

$$\frac{\mathcal{c}_m}{20\log_{10}(e)} = \begin{cases}-\sum\limits_{i=1}^{\infty}J_0(i\tilde{A})\frac{G^i}{i}\cos(i\psi), & m=0\\ 2\sum\limits_{i=1}^{\infty}J_m(i\tilde{A})\frac{G^i}{i}\sin(i\psi), & m \text{ odd}\\ -2\sum\limits_{i=1}^{\infty}J_m(i\tilde{A})\frac{G^i}{i}\cos(i\psi), & m \text{ even}\end{cases} \tag{20}$$

4 Model Evaluation

The derivations thus far are evaluated in the following subsections. First, they are used for making several observations about RSS-based respiration rate monitoring. Then, an empirical validation of the RSS model in Eq. (19) is given.

4.1 Numerical Evaluation

Suppose that the periodic movement represents respiration of a person, which is monitored by a TX-RX pair operating at 2.4 GHz ISM band so that $\lambda \approx 0.125$ m. Although the respiration has a non-trivial relation between sex, age, and posture [33], on average, it is a small quantity, for example, $A = 1$ centimeter maximum displacement[8]. An example deployment of such a system is expected to yield RSS measurements shown in Fig. 2.

A closer look at the coefficients in Eq. (20) reveals that when $\Delta \approx n\lambda/2$ for any integer n, all odd order harmonics $\mathcal{c}_{2m-1}$ get closer to 0 due to $\sin(n\pi)$ product. Similarly, when $\Delta \approx n\lambda/4$ for odd n, all even order harmonics $\mathcal{c}_{2m}$ get closer to 0. Therefore, for some special values of initial excess path value Δ_0, the breathing of a stationary person may exhibit only even or odd harmonics in their measurement signal. The same argument is true for RSS measurements in linear scale (see Eq. (14)), and it is independent of the actual periodic breathing signal function. In Fig. 2b, Eq. (15) is used for calculating the RSS values for different Δ_0 values. It can be seen that when $\Delta_0 = 3\lambda/2$, the RSS has a smaller amplitude but double perturbation frequency. At these distances, it can be observed from Fig. 2e that the signal energy is very small.

The respiration signal in Eq. (13) (and Eq. (19)), is a series expansion of a frequency modulated signal. For frequency

8. This is an example value, and may not correspond to any specific combination of sex, age, and posture for a chest or abdominal movement associated with the respiration [33].

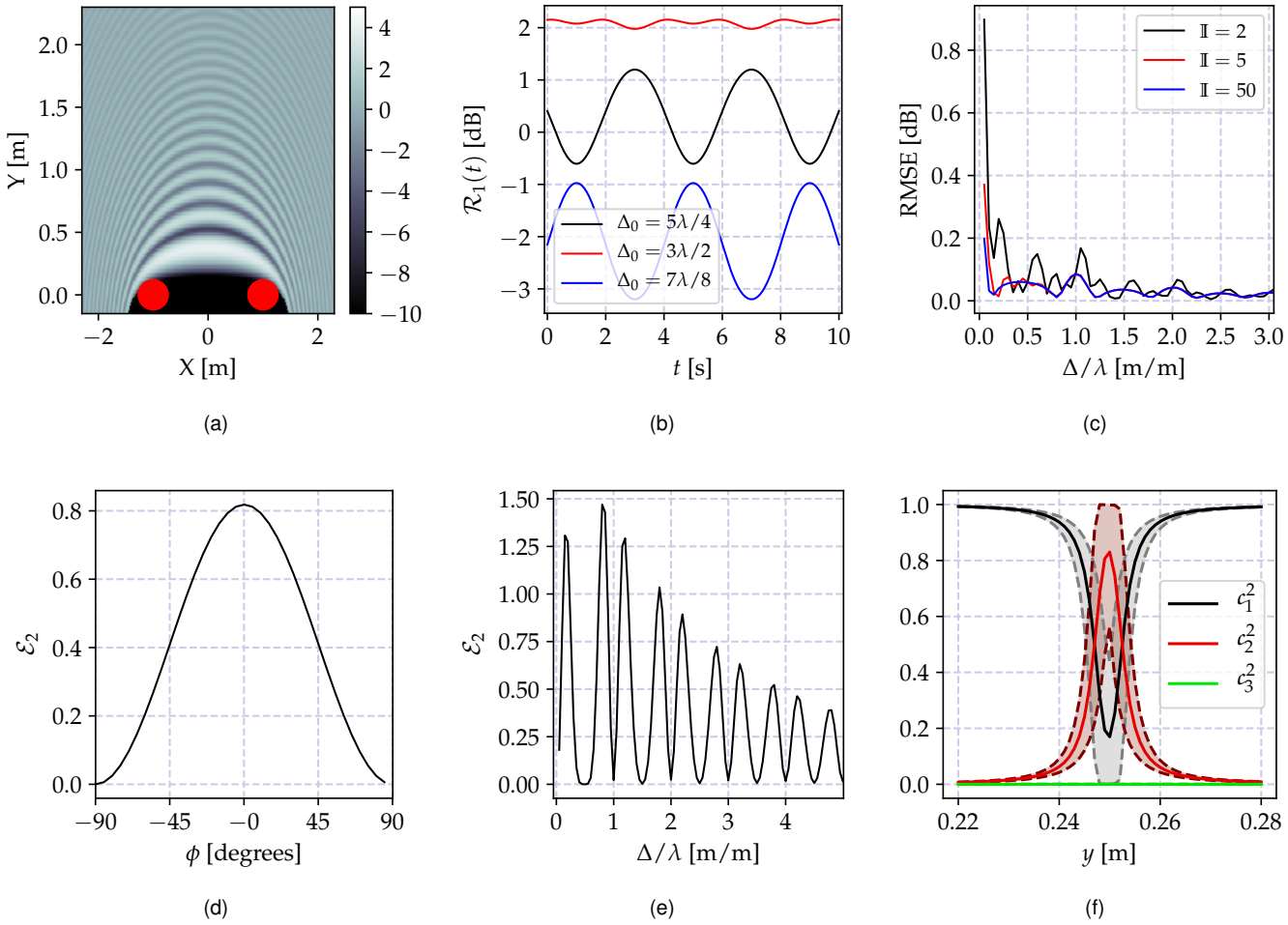

Fig. 2. The RSS and signal energy variation of a link with TX node at $\boldsymbol{p}_t = [-1, 0]^\top$ and RX node at $\boldsymbol{p}_r = [1, 0]^\top$ operating with wavelength $\lambda = 0.125$ m in an environment with path-loss exponent $\eta = 2$ when a circular object of radius 0.3 m and relative permittivity $\epsilon_r = 1.5$ moves to different positions. In (a), the variation of the RSS with the initial object's position $\boldsymbol{p}_0$. In (b), the variation of RSS when the object perturbs the RSS with a sinusoidal movement in direction $\boldsymbol{\delta} = [0, -1]^\top$ and amplitude $A = 0.01$, and the object's initial positions on $x = 0$ line with y axis yielding the specified excess path lengths Δ_0. In (c), the variation of RMS error between the model output in Eq. (15) and approximation using two harmonics and $\mathbb{I}^{\text{th}}$ order series in coefficients in Eq. (20). In (d), the variation of the signal energy with the orientation of the perturbation direction defined as $\phi = \arccos([0, -1]^\top \boldsymbol{\delta})$ when $\Delta_0 = \lambda/4$ meters and the person is on the $x = 0$ line. In (e), the variation of the signal energy $\mathcal{E}_2$ with the wavelength normalized excess path length Δ/λ. In (f), the relative contribution of harmonics to the signal energy for the object in Fig. 2 when it is moving on the mid-line between TX and RX ($x = 0$) for the specified y-axis values. In the plots of (f), the coefficients are normalized with $\hat{c}_m^2 = c_m^2/\mathcal{E}_3$. The shaded areas between dashed lines are the coefficient square values for 16 frequency channels separated by 5 MHz, and the solid lines are their means.

modulated signals, the number of terms in their series expansion can be found by Carson's bandwidth rule [31, ch. 5], which states that it is enough to consider only $2(\tilde{A}/2\pi + f)$ harmonics of the Fourier series in Eq. (12). Since the maximum displacement due to respiration can be assumed to satisfy $A = 0.01$ m, and its frequency can be assumed to be less than 30 breaths per minute (0.5 Hz), as it has been done earlier [8], [9], Carson's rule implies that only two harmonics are needed to represent most of the signal. Consequently, a conservative approximation of the amplitude ratio in linear scale R and in logarithmic scale $\mathcal{R}$ is obtained by truncating the series in Eq. (13) at the second term. For lower respiration rates, it is possible to truncate the series after the first term and obtain a single tone approximation which was used in the previous works, e.g., [9].

The infinite series in Eq. (17) can be truncated at lower orders if the total signal energy is concentrated greatly in lower order harmonics. For this purpose, one can invoke Parseval's Theorem to find the signal energy of $\mathcal{R}$ from the periodic series expansion in Eq. (17) as

$$\mathcal{E}_{\mathcal{R}} \triangleq \sum_{i=1}^{\infty} \frac{G^{2i}}{i^2} = \text{Li}_2(G^2),$$

where $\text{Li}_2(\cdot)$ is the *di-logarithm* function [34]. Then, the total signal power is monotonically increasing with G. Since G, defined in Eq. (6), is a decreasing function of Δ and an increasing function of Γ, it attains its maximum when $\Delta = 0$ so that $\text{Li}_2(G^2) \leq \text{Li}_2(\Gamma^2)$. This implies that the signal energy is concentrated at the lower order harmonics if Γ is lower than 1, which is defined by the incidence angle θ_i (cf. Fig. 1) and the object's relative permittivity. When the reflector object is close to the link-line, θ_i approaches 0 radians, making Γ very close to 1. In this case, more than

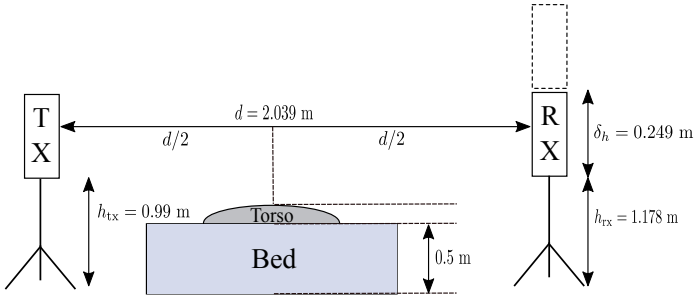

Fig. 3. The experimental setup where a person breaths at a constant rate of 15 BPM when a pair of nodes operate at 868 MHz

two terms are needed to reach a good approximation of the series in Eq. (20). However, when the object is sufficiently far away from the link-line, Γ assumes smaller values and Δ increases, making G a small quantity. When G is smaller than 0.7, the first two harmonics in Eq. (17) contain 96.76% of the total signal energy $\mathcal{E}_{\mathcal{R}}$, making a two term approximation a reasonable choice. The variation of root-mean-square error (RMSE) with excess path length Δ is depicted in Fig. 2c for different truncation orders of the series in Eq. (20) while using only the first two harmonics in Eq. (19). As shown, even for small Δ, the two term series truncation yields small error.

Consider the signal energy of the approximate N harmonics signal, which is given by

$$\mathcal{E}_N \triangleq \sum_{i=1}^{N} c_i^2. \tag{21}$$

Its variation with the direction of the perturbation and the wavelength normalized excess path length Δ/λ are depicted in Fig. 2d and Fig. 2e respectively. As shown, the energy may significantly change with the object's orientation and position. One consequence of this result is that there are certain positions where small changes drastically degrades the SNR. For example, when the object in Fig. 2 is moving on the mid-line between TX and RX nodes, at certain y-axis values, the relative importance of the second harmonic exceeds the first harmonic as shown in Fig. 2f. When excess path length is close to such a value, even small wavelength variations may change the SNR of the measurements as can be observed from the plots in the figure. Furthermore, any uncertainty in electrical parameters of the object or its geometry increases the uncertainty further. Therefore, the SNR is a statistical quantity, and it is tedious to compare the model output with the measurement data.

4.2 Empirical Validation

The RSS model in equations (19) and (20) is derived after making several simplifying assumptions on the respiration movement itself. In this regard, it is implicitly assumed that the absolute energy of the respiration signal is not of particular interest for RSS-based respiration rate monitoring, but only its relative magnitude compared to the noise power. Correspondingly, the proposed model can be validated by comparing the variation of the measured energy of the first harmonic $\mathcal{E}_1$ with the expected variation.

In order to demonstrate the validity of the model predictions, an experiment setup visualized in Fig. 3 is used for acquiring RSS measurements of a TX-RX pair operating at 868 MHz using the high granularity RSS acquisition system presented earlier in [29]. The TX node emits a continuous wave at 868 MHz while the RX node captures 100 of the in-phase and quadrature samples, which are then used for calculating RSS approximately every 1.6 milliseconds.

The experiment is repeated with four different people, who have different sizes and different breathing amplitudes. The people are three male (Person 1, 2, and 4 in Fig. 4) and one female (Person 3 in Fig. 4) healthy adults of different ethnicity, and between 23 and 34 years old. During the experiment, each person is breathing at a constant rate of 15 breaths-per-minute (BPM). In order to alter the excess path length, the receiver antenna height (distance to the ground) is incremented by 2.49 centimeter intervals in the direction shown in Fig. 3. The RX acquires the RSS measurements for 30 seconds, before its height is incremented. The RX height is increased in total by $\delta_h = 0.249$ meters.

The acquired RSS data is used for calculating the energy of the first harmonic $\mathcal{E}_1$, which is approximated by the signal energy within 0.25 ± 0.03 Hz band of the spectrum. The variation of $\mathcal{E}_1$ with the wavelength normalized excess path length Δ/λ corresponding to each RX height is shown in Fig. 4. The amplitude of the energy is defined by unknown factors, and strongly depends on the person as shown in the figure. However, the energy has a sinusoidal variation with Δ/λ as the expression for $m = 1$ in Eq. (20) implies, and the fitted sinusoids in Fig. 4 show. As expected, this variation can be observed for all people regardless of their gender, physical properties or age. Therefore, the SNR variation is a common phenomenon for RF-based respiration rate systems, and must be evaluated for a deployment to achieve successful respiration rate monitoring.

4.3 Discussion

In this section, several implications of the model are discussed. We first elaborate on the physical parameters defining the SNR, and then, derive the impact of the linear movements of a breathing person. Finally, we give a summary of the findings.

4.3.1 Impact of physical parameters

The observed breathing signal amplitude, and the SNR, depends on the effective amplitude of the breathing displacement $\tilde{A}$ defined in Eq. (11), effective reflection coefficient G defined in Eq. (6), the excess path length when the person is in the initial position $\boldsymbol{p}_0$, and the wavelength λ. The relative importance of these parameters can be investigated by considering the series coefficients in equations (14) and (20). If we have $\Delta \ll d$, and for perpendicularly polarized propagation scenario, the SNR is a function of ψ and $\tilde{A}$, which are defined by the initial position $\boldsymbol{p}_0$, perturbation direction with respect to the link-line δ_Δ, the respiration amplitude A, and the wavelength λ. Therefore, for fixed λ and A, the position and orientation of the person are the most important parameters dictating successful respiration rate estimation.

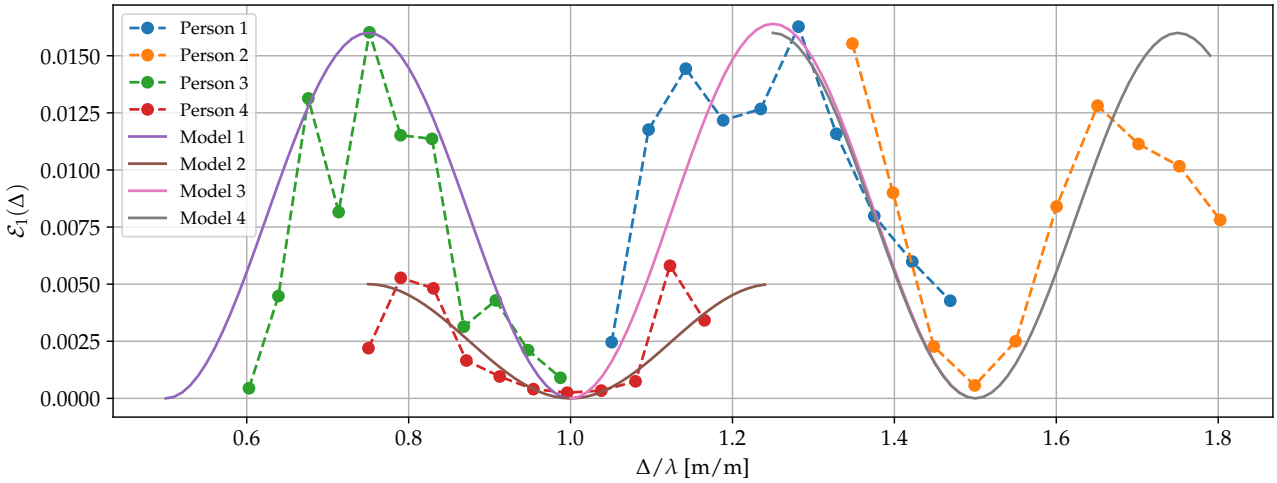

Fig. 4. The variation of energy of the first harmonic (at 0.25 Hz) for each person as the excess path length Δ changes due to lifting up the RX antenna in 10 (for people 1 and 2) and 9 (for people 3 and 4) equal steps of 2.49 centimeters.

Let us now suppose that A and λ are fixed, and we have $\Delta \ll d$. Then, the variation of the two harmonic signal energy $\mathcal{E}_2$, defined in Eq. (21), with the orientation of the perturbation direction are as shown in Fig. 2d. As the figure implies, when the perturbation direction gets tangential to the ellipses having the nodes at their foci, the SNR gets close to zero. In other words, the perturbation direction $\boldsymbol{\delta}$ must have a significant component normal to the ellipses in order to favor successful breathing rate estimation. Similarly, the evaluation in Fig. 2e implies that when the person's position is close to an integer multiple of $\lambda/2$, a low SNR is observed. For such Δ values, the first harmonic is very close to zero, and the second harmonic is expected to be significant. In this case, if the noise power is small, the second harmonic may be the strongest tone in the power spectral density of the measurements. Therefore, in high SNR conditions, estimators assuming presence of more than one harmonics are expected to perform better.

In order to investigate the position dependence of G defined in Eq. (6), it is enough to consider the variation of incidence angle θ_i with the position $\boldsymbol{p}$. It can be seen by inspecting its definition shown in Fig. 1 that we have

$$\begin{aligned} \theta_i &= \frac{\pi}{2} - \frac{1}{2}\arccos(p(\boldsymbol{p})), \\ p(\boldsymbol{p}) &\triangleq \left(\frac{\boldsymbol{p}-\boldsymbol{p}_r}{\|\boldsymbol{p}-\boldsymbol{p}_r\|}\right)^{\top}\left(\frac{\boldsymbol{p}-\boldsymbol{p}_t}{\|\boldsymbol{p}-\boldsymbol{p}_t\|}\right). \end{aligned} \tag{22}$$

Then, it follows from the definition of the Fresnel reflection coefficient that its first order Taylor series expansion reads as

$$\Gamma \approx \Gamma_0 - \Gamma_0 \frac{p(\boldsymbol{p}) - p(\boldsymbol{p}_0)}{\sqrt{(p^2(\boldsymbol{p}_0)-1) + 2(p(\boldsymbol{p}_0)+1)\epsilon_r}}, \tag{23}$$

where Γ_0 is the coefficient at initial position $\boldsymbol{p}_0$, and ϵ_r is the relative permittivity. When the object is between the nodes, and as it gets closer to the link-line $p(\boldsymbol{p})$ gets closer to -1, the rate of change of Γ increases so that small amplitude perturbations may significantly alter Γ. Therefore, when the person is very close the link-line, the respiration signal is also amplitude modulated due to variation of Γ, which alters the observed SNR.

Thus far, we have assumed that the reflection model is valid for the considered propagation scenario shown in Fig. 1, where the reflector object and the antennas are standing in $+z$ direction of the reference frame in the figure. Since the electric field generated by the transmitter antennas is perpendicular to the plane-of-incidence[9], only horizontally polarized reflection can take place. For this scenario, the distance of the person to the link-line is taken into account through the excess path length Δ. On the other hand, for the cases when the person is lying below the antennas, and antennas are not oriented for horizontal polarization, the reflected wave has both horizontally and vertically polarized components. Such a reflected signal experience additional losses due to polarization mismatch at the receiver antenna. Conversely, when the antennas are aligned to maximize the polarization match, the height of the antennas from the person's body only contributes to Δ, and the derived model is valid. Therefore, the SNR of the measurements are also functions of the polarization, and any mismatch degrades the achievable respiration rate estimation performance.

4.3.2 *Effects of linear movement*

In order to investigate the impact of linear movements on the breathing induced RSS variation, let us suppose that the object shown in Fig. 1 makes small periodic movements ($g(t)$) in addition to a constant velocity movement in another direction. In other words, at time instant t, the initial point $\boldsymbol{p}_0$ moves to $\boldsymbol{p}(t) = \boldsymbol{p}_0 + g(t)\boldsymbol{\delta} + \boldsymbol{v}t$, where $\boldsymbol{v}$ is the constant velocity with amplitude $v = \|\boldsymbol{v}\|$. If $g(t)$ has a small amplitude and t is close enough to the time epoch, the Taylor series expansion of the excess path length Δ is

9. The plane containing both the direction of propagation vector and the surface normal is defined as the *plane-of-incidence*. The interested reader is referred to [13, ch. 3] for a condensed summary of the propagation concepts.

valid, and for this case Eq. (8) can be written as

$$\Delta(\boldsymbol{p}) - \Delta_0 \approx \left[\frac{\boldsymbol{p}_0 - \boldsymbol{p}_r}{\|\boldsymbol{p}_0 - \boldsymbol{p}_r\|} + \frac{\boldsymbol{p}_0 - \boldsymbol{p}_t}{\|\boldsymbol{p}_0 - \boldsymbol{p}_t\|}\right]^\top [g(t)\boldsymbol{\delta} + \boldsymbol{v}t].$$

Similar to the definition in Eq. (9), let us denote the second inner product as

$$\delta_v = \left[\frac{\boldsymbol{p}_0 - \boldsymbol{p}_r}{\|\boldsymbol{p}_0 - \boldsymbol{p}_r\|} + \frac{\boldsymbol{p}_0 - \boldsymbol{p}_t}{\|\boldsymbol{p}_0 - \boldsymbol{p}_t\|}\right]^\top \boldsymbol{v},$$

so that $\Delta(\boldsymbol{p}) - \Delta(\boldsymbol{p}_0) \approx g(t)\delta_\Delta + \delta_v t$. Then, Eq. (5) becomes

$$\begin{aligned} R(\boldsymbol{p}) \approx & 1 + G^2(\boldsymbol{p}) - \\ & 2G(\boldsymbol{p}) \cos\left(2\pi\frac{1}{\lambda}(\delta_\Delta g(t) + \delta_v t) + \psi(\boldsymbol{p})\right), \end{aligned} \tag{24}$$

where the position dependence of R and phase ψ defined in Eq. (11), which cannot be ignored for this case, are explicitly written.

In case $g(t)$ is of the form $g(t) = A\sin(2\pi f t)$, then Eq. (24) can be written as

$$\begin{aligned} R_2 \approx & 1 + G^2(t) - \\ & 2G(t) \sum_{m=-\infty}^{\infty} J_m(\tilde{A}) \cos\left(2\pi\left(\frac{\delta_v}{\lambda} + mf\right)t + \psi\right), \end{aligned} \tag{25}$$

and in logarithmic scale it reads as

$$\begin{aligned} \mathcal{R}_2 \approx & -20\log_{10}(e) \sum_{m=-\infty}^{\infty}\sum_{i=1}^{\infty}\left\{J_m(i\tilde{A})\frac{G^i(t)}{i}\right. \\ & \left.\cos\left(2\pi\left(i\frac{\delta_v}{\lambda} + mf\right)t + i\psi\right)\right\}. \end{aligned} \tag{26}$$

Similar to Eq. (25), Eq. (26) can also be written in the form in Eq. (19) with the same coefficients in Eq. (20).

The derivations given above show that the linear movements shift the frequency of the periodic movement and make the effective reflection coefficient G defined in Eq. (6) a time varying quantity since $\delta_v t/d$ term in $\Delta(\boldsymbol{p})$ cannot be neglected. If this variation has a bandwidth higher than the respiration frequencies, the spectrum around integer multiples of δ_v/λ Hz are spread. Therefore, if there is a time variation in either direction or amplitude of the movement, RSS-based respiration rate monitoring is a prohibitively demanding task.

4.3.3 Summary

The analysis in the previous sections and the discussions above imply that:

i.) The RSS measurements in linear scale Eq. (13) and logarithmic scale Eq. (19) have similar forms.

ii.) The signal energy can be estimated using Eq. (21) for $N = 2$ as the higher order terms introduce small modeling error.

iii.) The breathing signal's energy has a non-trivial relation with the breathing direction with respect to the link-line, the breathing amplitude, the initial position of the person, person's body geometry, and the electrical properties of the person's clothes and body. Therefore, the SNR of the breathing signal is statistical, and some diversity mechanism is needed to improve breathing estimation quality. For example in [8] frequency diversity and in [9] spatial diversity are used. In works using CSI output of multiple input multiple output WiFi devices, the channel gains are estimated for large number of subcarriers and multiples of transmitter and receiver antennas, which yield improved breathing rate estimation quality.

iv.) The position of the person $\boldsymbol{p}_0$ and the breathing direction $\boldsymbol{\delta}$ are the most important parameters defining the SNR. Therefore, successful respiration rate monitoring requires that the person does not stay in the orientation or location yielding very low SNR, or the monitoring system should provide a diversity mechanism that enable simultaneous measurement acquisition from different locations and/or orientations.

v.) The polarization of the antennas, and the orientation of the person's surface with respect to the link-line are important, and may create polarization mismatch. When deploying a system, the antenna polarization and the expected alignment of the person must be taken into account.

vi.) When the object moves even with a constant velocity, the perturbation spectrum shifts depending on the speed and direction of the movement. In this case, the perturbation frequency estimate has a different nature and it is required to first estimate the center frequency δ_v/λ (see Eq. (26)). The other option is to stop estimating breathing rate when a movement is detected, as it has been done in [8].

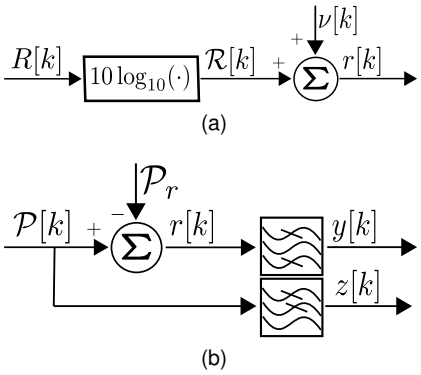

Fig. 5. In (a), relations between various parameters introduced in Sec. 3, and in (b), preprocessing of the RSS measurements

5 Breathing Rate Estimation

The analysis in the previous section conclude that the effect of respiration on RSS can be modeled in terms of the amplitude ratio in linear scale R defined in Eq. (5) and in logarithmic scale $\mathcal{R}$ defined in Eq. (15) along with the additive noise ν as shown in Fig. 5a.

In this section, we discuss three approaches to estimate the respiration rate f. The estimators given in this section do not use the RSS measurement $r[k]$ directly, but its bandpass filtered version $y[k]$ or low-pass filtered $\mathcal{P}[k]$, denoted as $z[k]$. These processing steps are visualized in Fig. 5b. The breathing rate estimation problem can be casted as single tone parameter estimation of a deterministic sinusoid using discrete observations as has been done in the related works [8]–[10]. The problem has been extensively studied due to its importance in various application areas [35, ch. 13]. In the first subsection, we give an overview of

the batch-based frequency estimation technique. Then, we discuss a Bayesian formulation of the same approach, and summarize its recursive solution from the work by Qi et al. [36]. Finally, we review a recently introduced model-based approach [16].

5.1 Batch Spectral Analysis

The most straight forward and standard approach in the literature for estimating the frequency of a single tone sinusoid is to perform spectral analysis using a batch of measurement data. For this purpose, the maximum and minimum breathing rates (perturbation frequencies) can be used for bandpass filtering the measurements $r[k]$ as shown in Fig. 5b. Then, the output signal $y[k]$ is split into M windows of length N_w with overlap N_o such that the data for the m^{th} window (for $m = 1, \ldots, M$) is given by

$$\boldsymbol{y}_m = \begin{bmatrix} y[n+1] & y[n+2] & \ldots & y[n+N_w] \end{bmatrix}^\top, \tag{27}$$

where the offset is $n = (m-1)(N_w - N_o)$. Then, from Eq. (27), the power spectral density (PSD) is estimated as

$$\boldsymbol{S}_m[l] = |\boldsymbol{Y}_m[l]|^2, \tag{28}$$

where $\boldsymbol{Y}_m[l]$ is the Discrete Fourier Transform (DFT) of $\boldsymbol{y}_m$. The l^{th} frequency is given by

$$f_l = \frac{l f_s}{N_w}, \tag{29}$$

where f_s is the sampling frequency and $l = 0, \ldots, N_w - 1$.

Eq. (28) naturally yields the whole spectrum for all frequencies f_l. In order to obtain a point estimate $\hat{f}$, the frequency corresponding to the maximum of the PSD is chosen, that is

$$\hat{l} = \underset{l}{\operatorname{argmax}}\, \boldsymbol{S}_m[l], \qquad \hat{f}_{\text{DFT}} = \frac{\hat{l} f_s}{N_w}, \tag{30}$$

excluding the DC component.

5.2 Recursive Bayesian Spectral Analysis

An alternative approach to the batch estimator given above is to use equivalent Bayesian formulation for spectral analysis. Since this method can cope with the DC term, we use the low-pass filtered data $z[k]$. The Bayesian recursive method starts with writing $z[k]$ in terms of its Fourier series expansion as

$$\begin{aligned} z[k] = a_0[k] + \sum_{n=1}^{N_{\text{KF}}} \Big\{ & a_n[k] \sin(2\pi f_n t_k) \\ & + b_n[k] \cos(2\pi f_n t_k) \Big\} + \tilde{\nu}[k] \end{aligned} \tag{31}$$

where N_{KF} is the number of frequency bins, $a_0[k]$, $a_n[k]$, and $b_n[k]$ are the time-varying Fourier coefficients with slight abuse of notation, f_n are the frequency bins, and $\tilde{\nu}[k] \sim \mathcal{N}(0, \sigma_\nu^2)$ is the measurement noise which is a filtered version of $\nu[k]$, but still assumed to be white.

Let $\boldsymbol{x}[k] = \begin{bmatrix} a_0[k] & \ldots & a_N[k] & b_1[k] & \ldots & b_N[k] \end{bmatrix}^\top$ be the vector of the Fourier coefficients, which are assumed to evolve as a Gaussian random walk according to

$$\boldsymbol{x}[k] = \boldsymbol{x}[k-1] + \boldsymbol{w}[k] \tag{32}$$

where $\boldsymbol{w}[k] \sim \mathcal{N}(0, \boldsymbol{C}_w)$ is the process noise with covariance matrix $\boldsymbol{C}_w$. Furthermore, assume that the initial state $\boldsymbol{x}[k]$ is distributed according to $\boldsymbol{x}[0] \sim \mathcal{N}(\boldsymbol{m}_0, \boldsymbol{P}_0)$.

Combining Eq. (31) and Eq. (32), the following linear state space model is obtained

$$\boldsymbol{x}[k] = \boldsymbol{F}\boldsymbol{x}[k-1] + \boldsymbol{w}[k], \tag{33a}$$
$$z[k] = \boldsymbol{G}\boldsymbol{x}[k] + \nu[k], \tag{33b}$$

where $\boldsymbol{F} = \boldsymbol{I}_{2N+1}$ is the $(2N+1) \times (2N+1)$ identity matrix and $\boldsymbol{G}$ is the $1 \times 2N+1$ dimensional observation matrix with the i^{th} component g_i defined as

$$g_i = \begin{cases} 1, & i = 1, \\ \sin(2\pi f_{i-1} t_k), & 1 < i \leq N_{\text{KF}} + 1, \\ \cos(2\pi f_{i-N_{\text{KF}}-1} t_k), & N_{\text{KF}} + 1 < i \leq 2N_{\text{KF}} + 1. \end{cases}$$

The linear model in Eq. (33) can then be used in a Kalman filter [37] to obtain recursive estimates of the Fourier coefficients $\boldsymbol{x}[k]$ at each time t_k. Finally, a point estimate of the breathing frequency is obtained in the same way as for the spectrum based method, that is, by selecting the frequency with highest magnitude such that

$$\hat{f}_{\text{KF}} = \underset{n}{\operatorname{argmax}} \sqrt{a_n^2 + b_n^2}, \qquad n > 0. \tag{34}$$

5.3 Model-based Estimation

The non-parametric statistical models can be used for capturing the effects of all the uncertainty sources affecting the SNR of the signal. One approach that has been recently introduced in [16] is to model the low-pass filtered RSS $z[k]$ (see Fig. 5b) as a quasi-periodic Gaussian process [38], [39], such that

$$z[k] = g[k] + \nu[k], \tag{35a}$$
$$g(t) \sim \mathcal{GP}(0, K(\tau)), \tag{35b}$$

where $g[k] \triangleq g(t_k)$ is the k^{th} sample acquired at time t_k, and $\mathcal{GP}(m(t), K(t, t'))$ denotes a Gaussian process prior with mean function $m(t)$ and covariance kernel $K(t, t') = K(t - t')$, and $\tau = t - t'$ [38]. For a temporal Gaussian process with the canonical periodic covariance function given by

$$K(\tau) = \sigma_K^2 \exp\left(-\frac{2\sin^2\left(\frac{2\pi f \tau}{2}\right)}{\ell^2} \right), \tag{36}$$

it can be shown that the following equivalent discrete-time state-space formulation

$$u_0[k] = u_0[k-1] + w_0[k], \tag{37a}$$
$$\boldsymbol{u}_n[k] = \boldsymbol{F}_n \boldsymbol{u}_n[k-1] + \boldsymbol{w}_n[k-1], \tag{37b}$$
$$g[k] = u_0[k] + \sum_{n=1}^{\infty} \boldsymbol{H}_n \boldsymbol{u}_n[k] \tag{37c}$$

can be obtained [16], [39]. In Eq. (36) σ_K^2 (variance), ℓ (length scale), and f (perturbation frequency) are hyperparameters. In Eq. (37), $u_0[k]$ is the DC component, $\boldsymbol{u}_n[k]$ (for $n > 0$) is a 2×1 vector containing the instantaneous value of the n^{th} harmonic and its derivative, $w_0[k] \sim \mathcal{N}(0, C_{w_0})$ and

$w_n[k] \sim \mathcal{N}(0, \boldsymbol{C}_{w_n})$ are the corresponding process noises, and

$$\boldsymbol{F}_n = \begin{bmatrix} \cos(2\pi f_n \delta_t) & -\sin(2\pi f_n \delta_t) \\ \sin(2\pi f_n \delta_t) & \cos(2\pi f_n \delta_t) \end{bmatrix}, \tag{38a}$$

$$\boldsymbol{H}_n = \begin{bmatrix} 1 & 0 \end{bmatrix}, \tag{38b}$$

$$\boldsymbol{C}_{w_n} = 4\delta_t \sigma_K^2 \exp(-\ell^{-2}) \mathcal{I}_n(\ell^{-2}) \boldsymbol{I}_2, \tag{38c}$$

$$C_{w_0} = 2\delta_t \sigma_K^2 \exp(-\ell^{-2}) \mathcal{I}_n(\ell^{-2}), \tag{38d}$$

where $\mathcal{I}_n(\cdot)$ is the n^{th} order modified Bessel function of the first kind, and $\delta_t = t_k - t_{k-1}$. The initial states are given by $\gamma_0[0] \sim \mathcal{N}(0, P_{0,\gamma_0})$ and $\boldsymbol{u}_n[0] \sim \mathcal{N}(0, \boldsymbol{P}_{0,\boldsymbol{u}_n})$.

Additionally, the logarithm of the breathing frequency $s[k] = \log(f[k])$ is modeled as a geometric Brownian motion which yields [40]

$$s[k] = s[k-1] - \frac{1}{2} S_f^2 \delta_t + w_s[k], \tag{39}$$

where S_f is the spectral density of the underlying white noise process and $w_s[k] \sim \mathcal{N}(0, S_f \delta_t)$.

Finally, combining Equations (35), (37), and (39), and truncating the series in Eq. (37c) at some upper bound N_{GP}, the following nonlinear state-space model is obtained

$$\begin{bmatrix} s[k] \\ u_0[k] \\ \boldsymbol{u}_1[k] \\ \vdots \\ \boldsymbol{u}_{N_{\text{GP}}}[k] \end{bmatrix} = \begin{bmatrix} s[k-1] - \frac{1}{2} S_f^2 \delta_t \\ u_0[k-1] \\ \boldsymbol{F}_1 \boldsymbol{u}_1[k-1] \\ \vdots \\ \boldsymbol{F}_{N_{\text{GP}}} \boldsymbol{u}_{N_{\text{GP}}}[k-1] \end{bmatrix} + \begin{bmatrix} w_s[k] \\ w_0[k] \\ \boldsymbol{w}_1[k] \\ \vdots \\ \boldsymbol{w}_{N_{\text{GP}}}[k] \end{bmatrix}, \tag{40a}$$

$$z[k] = u_0[k] + \sum_{n=1}^{N_{\text{GP}}} \boldsymbol{H}_n \boldsymbol{u}_n[k] + \nu[k], \tag{40b}$$

where the dependence of the matrices $\boldsymbol{F}_n$ on $s[k]$ is implicit. The model Eq. (40) can now readily be used in a (nonlinear) Kalman filter such as the unscented Kalman filter or extended Kalman filter [37]. In this paper, we use Rao–Blackwellized unscented Kalman Filter presented earlier in [16]. Finally, the frequency estimate is given by

$$\hat{f}_{\text{GP}} = \exp(\hat{s}), \tag{41}$$

where $\hat{s}$ is the first component of the latest state estimate.

5.4 Discussion

In this section, three different methods for estimating the frequency of periodic signals are summarized. All the methods are available in the literature, and they have been successfully applied for respiration rate monitoring. Here, we compare the advantages and shortcomings of the methods in order to aid the practitioners to select appropriate method for a deployment.

It is well established that the maximum likelihood estimate of the frequency of an unknown sinusoid is the bin of the peak of the periodogram [11]. The peak of the periodogram can be calculated using fast Fourier transform (FFT) algorithm. However, this method is subject to thresholding affect, and requires high SNR for a good performance. In high SNR regime, a course FFT of the measurements can be calculated and the estimate can be improved using three of Fourier coefficients [41] or using three samples directly in the DFT domain [42]. However, this method can only be applied if the data are evenly sampled, and it requires significant memory and processing power to calculate the complete spectrum.

Rather than processing entire overlapping windows at a time, the spectrum can also be estimated by using a recursive Bayesian spectrum estimation approach [36]. This method can cope with the DC term since it is possible to choose the resolution and sampling rate. Once these parameters are selected, the dimension of the state space can be controlled by shrinking the spectrum by low-pass filtering the measurements. This method has all the advantages of recursive implementations including decreased computational and memory requirements. In addition to these, an important advantage of this method compared to the batched DFT-based approach is its capability of working with unevenly sampled data. Therefore, this method is a better option for estimating the peak of the PSD.

Both of the DFT-based methods require to estimate the complete spectrum of the measurements. These methods operate on individual time series, and require an additional step to combine measurements from different sources, e.g., measurements from different antennas or communication channels. These problems can be addressed by using a model based estimator. In principle, the model of the RSS measurements in Eq. (13) and Eq. (19) could be exploited to improve the perturbation frequency estimation or to relax the requirements of the DFT-based (both batch or recursive) estimators. However, since the small perturbations depend on many different parameters such as the breathing direction with respect to link-line, breathing amplitude, initial position of the person, their geometry, and electrical properties of their clothes this option is non-trivial. Instead, non-parametric statistical models can be used for capturing these effects while providing the benefits of model based estimators. This approach has recently been presented in [16] by modeling the underlying signal as a quasi-periodic Gaussian process. The model summarized in the previous subsection can handle unevenly sampled data due to missing or dropped packets, include more than one harmonics into the model, and can readily combine measurements from different sources to obtain optimal estimates without explicit spectrum estimation. However, as with other recursive methods, it requires a good initial estimate in order to guarantee convergence in acceptable number of iterations.

In summary, the DFT-based methods require one to define the resolution of the spectrum estimates, and may need an additional step to improve the estimate accuracy. Although the recursive solution can handle missing packets, both of the DFT-based methods require an additional procedure to combine measurements from different sources. These methods can provide an estimate regardless of the SNR, although the performance can quickly degrade below a threshold. All the problems of DFT-based methods are addressed by non-parametric statistical model based estimator, which also enable inclusion of more than one harmonics into formulation in high SNR conditions. However, a good initial solution must be provided in order to guarantee convergence in reasonable number of iterations. Therefore, when SNR is low, a DFT-based estimator, in particular recursive Bayesian estimator, is a better option; on the contrary, when

TABLE 1
Evaluation Parameters

Symbol	Value	Appearance	Explanation
f	Varying	Sec. 6.1	Breathing frequency in bpm
f_s	Varying	Sec. 6.1	Sampling frequency in Hz
N_{DFT}	2048	Eq. (28)	Number of FFT points
N_w	30 s data	Eq. (27)	FFT window length
N_o	$N_w - 1$	Eq. (27)	FFT window overlap
N_{KF}	75	Eq. (31)	Number of frequency bins in KF
$\boldsymbol{C}_w$	$0.01\boldsymbol{I}_{2N+1}$	Eq. (33)	Process noise covariance
$\boldsymbol{m}_{0,\text{KF}}$	$\begin{bmatrix} z[0] \\ 0 \\ \vdots \\ 0 \end{bmatrix}$	Eq. (33)	Initial estimate of KF
$\boldsymbol{P}_{0,\text{KF}}$	$\boldsymbol{I}_{2N+1}$	Eq. (33)	Covariance of the initial estimate
N_{GP}	2	Eq. (31)	GP Truncation Order
σ_K^2	0.01	Eq. (36)	Covariance kernel variance
ℓ	0.9	Eq. (36)	Covariance kernel length scale
S_f	10^{-4}	Eq. (39)	White noise process PSD
δ_t	$1/f_s$	Eq. (38)	Time difference between samples in seconds
P_{0,u_0}	$\sqrt{0.1}\boldsymbol{I}_2$	Eq. (38)	Covariance of the initial state estimate components corresponding to DC terms
$\boldsymbol{P}_{0,\boldsymbol{u}_n}$	$\frac{1}{2^n n!}\boldsymbol{I}_2$	Eq. (38)	Covariance of the initial state estimate components corresponding to non-DC terms
$\boldsymbol{m}_{0,\text{GP}}$	$\begin{bmatrix} \ln(15/60) \\ z[0] \\ 0 \\ \vdots \\ 0 \end{bmatrix}$	Eq. (40)	Initial estimate of GP
σ_ν^2	1	Various	Measurement noise variance for KF and GP models

SNR is high, model based estimator is a much better option as we demonstrate using empirical data in the next section.

6 Experimental Results

In this section, the developments of the paper are evaluated using experimental data. In the following, we present the experimental setup and overview of the experiments before introducing the evaluation metrics. Then, the results are given.

6.1 Experimental Setup and Experiments

The experiments are conducted using the nodes with the hardware and software platform described in [43]. A TX node is programmed to transmit packets over 16 frequency channels at the 2.4 GHz ISM band[10]. After each transmission, the frequency channel of communication is changed sequentially to cover the 80 MHz spectrum. The RX nodes are programmed to listen for ongoing transmissions. Upon reception, the packets are timestamped at the start of frame delimiter with a resolution of $1/32$ microseconds, and the received frames are stored to a non-volatile memory.

10. The developments presented thus far consider a stream of RSS measurements with constant wavelength. In this section, the acquired measurements from different frequency channels are considered as different measurements with different wavelengths.

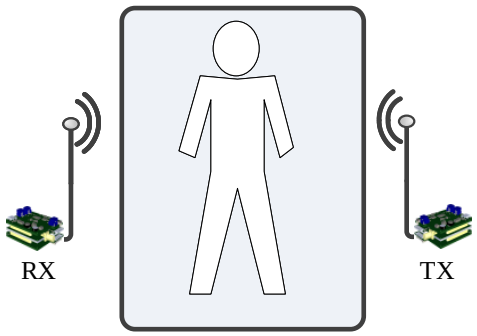

Fig. 6. The test setup of the bed experiment. A TX-RX pair of nodes are placed 2 meters apart from each other when a person is laying on their back and breathing at a specific rate set by a metronome.

The first experiment aims at evaluating the accuracy of the estimators and the experimental procedure is the same as the experiment no. 1 in [8]. The RSS measurements are acquired by a single RX node, which is 2 m away form the TX node, and 20 centimeters above the chest height of the person as shown in Fig. 6. The setup is deployed in a bedroom of an apartment, which is furnished with a wardrobe, nightstands, and other furnitures. The experiment is conducted in a typical apartment, where more than ten WiFi networks are identified to co-exist with the system. The transmission interval is set to 2 milliseconds so that $f_s = 31.25$ Hz for each frequency channel. During the experiments the person is lying on a bed while breathing at a constant rate set by a metronome for two minutes. The person breaths at 5 different rates: $12, 14, 16, 18$ and 20 breaths-per-minute (bpm). In total 80 time series are recorded and used for the evaluation. We refer to this experiment as the *bed experiment*.

The second experiment aims at evaluating how the SNR impacts estimation performance. The TX node emits frames every 1.92 milliseconds, and 11 RX nodes acquire the RSS variation when the person is standing in four different positions as shown in Fig. 8a. The setup is deployed in a large empty room of an office building, where several WiFi networks co-exist with the system. The nodes are placed on tripod stands approximately 85 cm above the ground. The positions of the person are selected such that different RX nodes observe different excess path length and direction of the breathing. This way a rich set of measurements are acquired to make conclusive statements about the model implications. At each position, the person is standing still while breathing at a constant rate of 12 bpm by following the breathing pace set by a metronome for one minute. The setup is also used for acquiring RSS measurements when the environment is empty. In total 176 time series are recorded for each position so that the evaluation is based on 704 data series. We refer to this experiment as *room experiment*.

In both of the experiments, the breathing person is a 35 years old healthy adult male. He is trained to follow the breathing pace set by the metronome before the experiments. Both of the experiments are conducted in public buildings, where presence, motion, or actions of other people in other rooms are not controlled. Furthermore, the operations of other wireless networks (in particular WiFi) operating in the same frequency band are not constrained. Although these WiFi networks create interference to the IEEE 802.15.4 devices, the measurements are acquired only when a complete frame can be decoded by the receiver. This approach guarantees that when bursty WiFi traffic interferes with the network operation, the frame is lost and no highly interfered measurement is acquired.

The acquired RSS data is preprocessed for each frequency channel measurement streams independently as shown in Fig. 5b. The bandpass filtered data $y[k]$ is obtained as output of two processing stages: first the mean is calculated and removed from measurement $\mathcal{P}[k]$, and then the result is low-pass filtered. The low-pass filtered data $z[k]$ is obtained by just low-pass filtering $\mathcal{P}[k]$. The used low pass filter is a 5^{th} order elliptic filter that has passband frequency of 2 Hz and stop frequency of 3 Hz, 0.05 dB maximum ripple in the pass band, and 40 dB stop band attenuation.

6.2 Evaluation Methodology

During the evaluation, we refer to the output of the batch estimator summarized in Sec. 5.1 as DFT estimate, the recursive Bayesian estimator presented in Sec. 5.2 as Kalman Filter (KF) estimate, and finally, the model-based estimator presented in Sec. 5.3 output is referred to as Gaussian Process (GP) estimate. These methods are implemented using the parameters tabulated in Table 1. All the methods are operated in single stream mode so that the number of estimates are equal and a sophisticated estimation combination procedure is not required.

The evaluation in this section is based on mean absolute error (MAE) calculations. For the breathing frequency estimation, the MAE in bpm is defined as

$$\varepsilon_f \triangleq \frac{60}{K}\sum_{k=1}^{K}|\hat{f}[k]-f|, \tag{42}$$

where f is the true rate, and $\hat{f}[k]$ is the k^{th} frequency estimate out of K total estimates. This metric fails to provide a measure of the dispersion in the estimates. For this purpose, we use the ratio of estimates within 1 bpm neighborhood of the true frequency f

$$\varepsilon_{\%} \triangleq \frac{\text{\# of } \hat{f} \text{ in 1 bpm neighborhood of } f}{\text{\# of estimates}} \cdot 100. \tag{43}$$

In order to quantify the convergence speed of the methods, we calculate ε_f for the data in the first 30 seconds and for the data afterwards separately. We refer to the former as $\varepsilon_f(t \leq 30\,\text{s})$ and the latter as $\varepsilon_f(t > 30\,\text{s})$. When the estimates have some outliers, e.g. they converge to the second harmonic frequency, we also calculate ε_f by excluding those outliers, and refer the result with ε_f *w/o outliers*.

In high SNR conditions, the ε_f performance of all the estimators are similar. In this case, the MAE of the estimated signal and the estimator input can be used for evaluation, since the estimator outputs also imply a signal in a specific form. Let us denote the model output of any estimator[11] as $\hat{\mathcal{R}}$. Then, we define the modeling MAE as

$$\varepsilon_z = \frac{1}{K}\sum_{k=1}^{K}|z[k]-\hat{\mathcal{R}}[k]|, \tag{44}$$

where for DFT-based method we add the mean value subtracted in the preprocessing stage.

The room experiment is used for evaluating the performance of the estimators under varying SNR conditions. The SNR of the signal is estimated using the PSD estimate in Eq. (28), using the actual breathing frequency. Let set $\mathcal{L}(f)$ contain the indices of the bins that are in a neighborhood of the harmonics of the true breathing frequency, excluding the DC term, and $\mathcal{S}$ denote the bins within interval 0.1 and 3 Hz, which define the frequency range we are interested in. Then, an SNR estimate is given by

$$\hat{\varrho} \triangleq 10\log_{10}\left\{\sum_{l\in\mathcal{L}(f)}\boldsymbol{S}[l]\Big/\sum_{l\in\mathcal{S}/\mathcal{L}(f)}\boldsymbol{S}[l]\right\}, \tag{45}$$

where the sets are disjoint. In the following, we use only the first two harmonics when forming the set $\mathcal{L}(f)$, and all other spectral bins contribute to the noise power.

6.3 Results

6.3.1 Bed experiment

In Fig. 7, breathing estimation is illustrated on two different frequency channels when the person is breathing at a constant rate of 0.2 Hz, that is, 12 bpm. The signal shown in Fig. 7a contains a strong first harmonic at the breathing frequency and all methods are capable of estimating the true frequency correctly as illustrated in Fig. 7d. The recursive GP and KF methods converge to the true frequency in approximately 15 s, whereas the DFT method requires 30 s because of the time window used to calculate the DFT. The breathing induced changes are not as evident for the signal shown in Fig. 7e since it contains higher order harmonics as proposed by the model and as illustrated in Fig. 7g. The KF and DFT methods estimate the breathing frequency using the peak of the spectrum, resulting in an incorrect estimate of $f \approx 24$ bpm which corresponds to the second harmonic. The higher order harmonics are taken into account in the GP-based estimator when truncation order is $N_{\text{GP}} > 1$. As a result, the method can correctly estimate the true breathing frequency as illustrated in Fig. 7h. The state estimates of the GP are illustrated in Fig. 7f and clearly, the method is able to track the DC-component and the harmonics accurately resulting in an improvement with respect to the spectral estimation techniques. For clarity, the second component of $\boldsymbol{u}_j$ is omitted from Figs. 7b and 7f.

The measurement setup of the bed experiment is a realization of the measurement setup evaluated in Fig. 2f. Thus, small displacements of the person, as can be observed in Fig. 2f, causes drastic changes in the SNR. Furthermore,

11. Although the state space models in Sec. 5 are different, all of these yield the same output form as in Eq. (19) only with different number of harmonics.

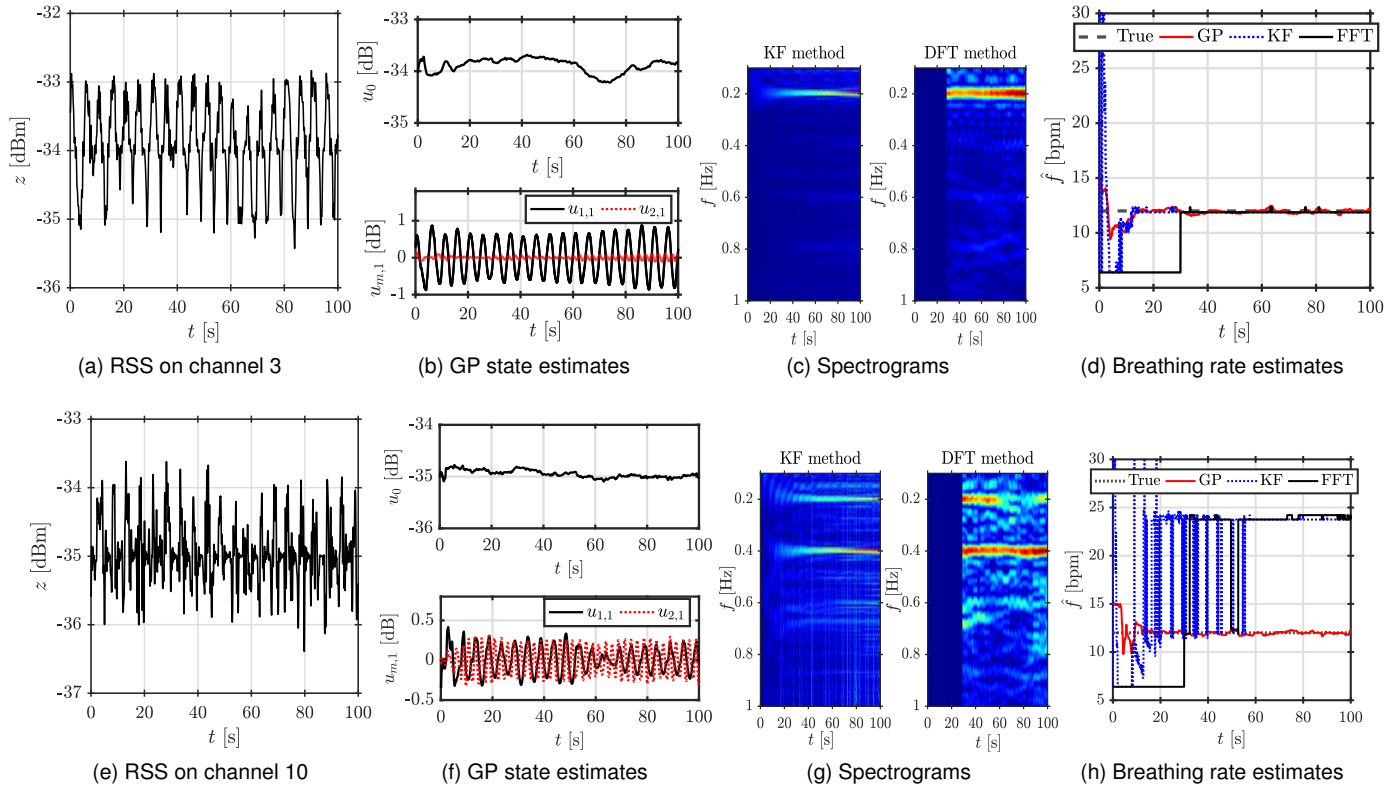

Fig. 7. Bed experiment: breathing monitoring on two different frequency channels using the presented methods. In (a) and (e), the breathing affected RSS signal. In (b) and (f), state estimates of the GP method ($N_{\text{GP}} = 2$). Spectrograms of the spectral estimation techniques illustrated in (c) and (g). The breathing rate estimates on the two channels are shown in (d) and (h).

TABLE 2
Results of the bed experiment

	GP	KF	DFT
$\varepsilon_{\%}$ [%]	97.50	88.75	87.50
$\varepsilon_f(t \leq 30\text{ s})$ [bpm]	1.06	5.10	-
$\varepsilon_f(t > 30\text{ s})$ [bpm]	0.25	1.44	1.41
ε_f w/o outliers [bpm]	0.15	0.25	0.26
ε_z [dB]	0.16	0.32	0.28

different frequency channel measurements may have different behavior as the spread of the shaded areas in the figure imply. For the acquired 80 signals, there are 8 signals having higher energy in the second harmonic. According to the evaluation in Fig. 2f, a particular y value (between 0.24 and 0.26 m) can yield such measurements. Therefore, the model correctly resembles this important scenario.

Performance of the estimators is summarized in Table 2 and on average, the spectral estimation techniques yield comparative accuracy while the GP-based estimator outperforms them. The ratio of valid estimates is summarized by $\varepsilon_{\%}$ and the 10% difference in favor of the GP method originates from the fact that the second harmonic has the highest amplitude in 8 out of 80 signals resulting incorrect estimates with the spectral techniques. The recursive GP and KF methods typically converge in the first 30 s and 75% of the estimates converge to within 1 bpm of the true rate in 15.8 s with GP and in 17.6 s with KF. However, the GP attains a significantly lower $\varepsilon_f(t \leq 30\text{ s})$ compared to KF, since the KF errors are typically very large due to the jumpy behavior as observed in Fig. 7d. After the transient period $(0 - 30\text{ s})$, the GP achieves a lower MAE than the spectral estimation techniques as given by $\varepsilon_f(t > 30\text{ s})$. However, these results are severely affected by the experiments that resulted in incorrect estimates due to measurements not showing the first harmonic, but the second one. Neglecting these outliers, one can observe that all methods yield comparative accuracy as given in the fifth row of Table 2. The steady-state accuracy of the spectral methods is mainly affected by the frequency bin size, whereas the GP accuracy could be improved by selecting the spectral density S_f smaller. However, this would also decrease responsiveness of the filter to possible breathing rate changes. Lastly, ε_z is given in the last row of Table 2. Clearly, the GP model estimates correspond more closely to the measured RSS since the higher order harmonics are taken into account.

The development in Sec. 3 concludes that the RSS is composed of more than one harmonics. However, the relative importance of the higher order harmonics depend on several factors, which include actual breathing function (in this regard it is evident that natural breathing is not a sinusoid) and effect of quantization in typical RSS measurement systems [27]. In order to quantify the importance of higher order harmonics, one may investigate the estimated energy in harmonics for all 80 time series. Since the model in Eq. (37c) is composed of Fourier series coefficients (and their derivatives), the relative energy in the m^{th} harmonic

TABLE 3
Truncation order

Truncation order N_{GP}	1	2	3	4
$\varepsilon_{\%}$ [%]	97.50	97.50	97.50	97.50
$\varepsilon_f(t > 30$ s) [bpm]	0.28	0.29	0.25	0.25
ε_z [dB]	0.19	0.17	0.16	0.16

TABLE 4
$\varepsilon_{\%}$ [%] with DFT method in room experiment

	Receiver number										
pos.	1	2	3	4	5	6	7	8	9	10	11
1	6	0	13	0	6	19	19	19	25	19	6
2	0	6	75	44	13	31	6	6	38	6	13
3	0	0	6	6	25	13	6	25	6	6	25
4	0	0	0	6	19	0	13	0	6	0	31

can be defined as

$$\mathcal{E}_{(m)} = u_{m,1}^2 \Big/ \sum_{n=1}^{4} u_{k,1}^2,$$

where $u_{m,1}$ denotes the first component of $\boldsymbol{u}_m$.

Averaging $\mathcal{E}_{(m)}$ across the 80 experiments results to $\mathcal{E}_{(1)} = 86.62\%, \mathcal{E}_{(2)} = 11.00\%, \mathcal{E}_{(3)} = 2.13\%$ and $\mathcal{E}_{(4)} = 0.25\%$, thus the first two harmonics contain approximately 98% of the energy. This value is very close to the value predicted by the Carson's rule of thumb, and implies that the actual breathing signal is a smooth function, not containing any jumps. Typically $\mathcal{E}_{(1)} \approx 93\%$, but it can be as low as 36% validating the importance of having an estimator that takes into account the higher harmonics. The accuracy of the GP with different truncation orders is given in Table 3. In terms of estimation accuracy, higher truncation order yields slightly better performance as indicated by $\varepsilon_f(t > 30$ s). In addition, ε_z is reduced with higher truncation order.

6.3.2 Room experiment

CDFs of the link SNRs for the room experiment are illustrated in Fig. 8b. The maximum SNR value for the empty room measurements is -12.42 dB and $7.4 - 25.0\%$ of the link SNRs exceeds this value when a breathing person is present. Thus, all positions clearly contain information regarding respiration rate of the person. However, SNR in the room experiments is typically much lower than in the bed experiment as shown in Fig. 8b.

The SNR of a link is defined by the signal energy $\mathcal{E}_1$ given in Eq. (21) for which the coefficients c_m can be calculated using Eq. (20). The coefficients c_m are functions of the effective reflection coefficient G defined in Eq. (6), and the effective amplitude of the periodic movement $\tilde{A}$ given in Eq. (11). The signal energy $\mathcal{E}_1$ increases as G increases, and G has its maximum when Γ is at its maximum on the link-line. In the room experiment, when the person is on position 1, G is in the interval $[0.02,\ 0.09]$ for the nodes 1 to 5, whereas for the nodes 7 to 11, $G \in [0.11,\ 0.23]$. As a result, the calculated signal energy $\mathcal{E}_1 = [0.02,\ 0.16]$ for the nodes 1 to 5 and $\mathcal{E}_1 \in [0.19,\ 0.23]$ for the nodes 7 to 11. With the nodes 1 to 5, the average SNR is -18.22 dB and $\varepsilon_{\%} = 5.0\%$ whereas with the nodes 7 to 11, the average SNR is -16.24 dB and $\varepsilon_{\%} = 17.5\%$. Thus, in position 1, it is expected that successful breathing monitoring is more likely with the nodes 7 to 11. The estimation results given in Table 4 are in accordance with this statement.

The effective reflection coefficient G is not the only parameter that affects the signal energy. In position 2, G is in $[0.21,\ 0.33]$ for the nodes 3 and 4, whereas for the nodes 7 and 8, $G \in [0.70,\ 0.94]$. Respectively, the effective perturbation amplitude $\tilde{A} \in [0.30,\ 0.54]$ for the nodes 3 and 4, it is in $[0.02,\ 0.12]$ for the nodes 7 and 8. Position 2 does not favor breathing monitoring for the nodes 7 and 8 despite that G is three times larger than it is for the nodes 3 and 4. The reason for this short coming is that breathing causes very small changes in the RSS of the nodes 7 and 8 and $\mathcal{E}_1 \in [0.00,\ 0.11]$, whereas for the nodes 3 and 4 the signal energy is $\mathcal{E}_1 \in [0.30,\ 0.86]$ due to the orientation of the person. Correspondingly, the average SNR of the nodes 3 and 4 is -10.53 dB and $\varepsilon_{\%} = 59.4\%$, whereas for the nodes 7 and 8 the average SNR is -15.88 dB and $\varepsilon_{\%} = 6.3\%$. These experimental results support the implications of the model.

It is important to keep in mind that a slight change in position or orientation can have a significant impact on the signal energy of the links and therefore, spatial diversity or frequency channel diversity must be used to increase the likelihood of successful breathing monitoring. Results for the different receivers and positions are summarized in Table 4. From the given results, it can be concluded that successful breathing monitoring is very likely across a large area as long as the position and orientation of the person yield SNR higher than -5 dB as in the bed experiment.

In Fig. 8c, the variation of $\varepsilon_{\%}$ of different estimators with the SNR is depicted. As shown, estimation accuracy of all three estimators improve when the SNR increases and $\varepsilon_{\%} = 100\%$ when SNR ≥ -4 dB. Although for the bed experiment GP outperforms the other estimators, its performance is lower when the SNR is low. In this region, the second and higher order harmonics have a lower power than the noise so that they are not as important as they are under the high SNR conditions. Correspondingly, the batch DFT method and recursive spectral estimators outperform the GP. This result suggests that for the low SNR operating region the batch DFT estimator is better whereas for the high SNR conditions the GP is better in terms of accuracy. It is also to be noted that GP has other advantages, the most notably it relaxes data acquisition requirements by not requiring uniform sampling, operating with occasional packet losses, and better fusing the measurements from different communication channels [16]. Therefore, it has an utmost importance to investigate the expected performance and to select an appropriate estimator for developing a robust and reliable RSS-based respiration rate monitoring system.

7 Conclusions

Breathing rate is an important vital sign of which continuous monitoring may help to identify serious problems before they actually occur. In this paper, a signal model for received signal strength based non-contact respiration rate monitoring systems using commodity wireless devices is presented.

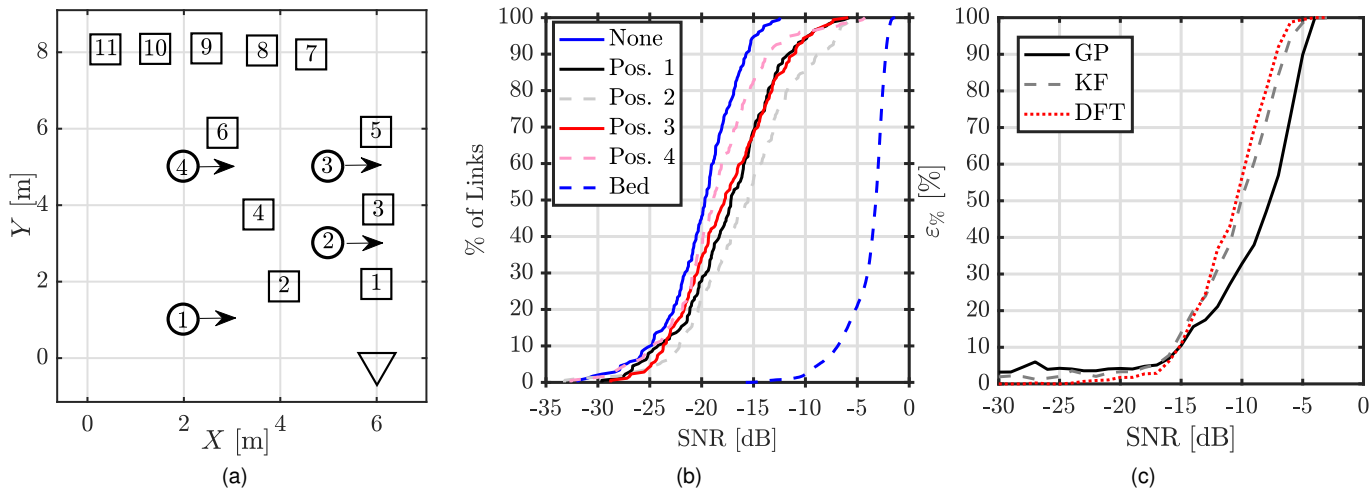

Fig. 8. In (a), layout of the room experiment, where ◯ is the position number of the person while facing to the direction shown with an arrow, □ is the receiver node identifier between 1 and 11, and finally ▽ is the transmitter node. CDF of link SNRs in different positions, including empty room (None) and bed experiment (Bed), are shown in (b). In (c), the variation of $\varepsilon_{\%}$ with SNR for the different estimators is shown.

It is shown that the signal model for low-end communication devices has the same form as the one in high-end radar based solutions. The effect of linear movement has also been derived, and significance of physical parameters are shown and discussed. Real world measurements are used for evaluating the performances of three previously presented estimators, and the result is compared with the implications of the model. The model implications are in coherence with the findings, and show that respiration rate monitoring systems must be evaluated before deployment. The estimator must be selected according to the expected signal-to-noise ratio of the measurements and the constraints imposed by the hardware and software implementations of the wireless nodes.

References

[1] M. A. Cretikos, R. Bellomo, K. Hillman, J. Chen, S. Finfer, and A. Flabouris, "Respiratory rate: the neglected vital sign," *Medical Journal of Australia*, vol. 188, no. 11, p. 657, 2008.

[2] J. F. Fieselmann and C. M. Helms, "Respiratory rate predicts cardiopulmonary arrest for internal medicine inpatients," *Journal of general internal medicine*, vol. 8, no. 7, pp. 354–360, 1993.

[3] F. Q. AL-Khalidi, R. Saatchi, D. Burke, H. Elphick, and S. Tan, "Respiration rate monitoring methods: A review," *Pediatric Pulmonology*, vol. 46, no. 6, pp. 523–529, 2011.

[4] E. F. Greneker, "Radar sensing of heartbeat and respiration at a distance with security applications," in *Proceedings of Radar Sensor Technology II (SPIE 3066)*, vol. 3066. SPIE, 1997, pp. 22 – 27.

[5] E. M. Staderini, "UWB radars in medicine," *IEEE Aerospace and Electronic Systems Magazine*, vol. 17, no. 1, pp. 13–18, Jan 2002.

[6] F. Adib, H. Mao, Z. Kabelac, D. Katabi, and R. C. Miller, "Smart homes that monitor breathing and heart rate," in *Proceedings of the 33rd Annual ACM Conference on Human Factors in Computing Systems*, ser. CHI '15. New York, NY, USA: ACM, 2015, pp. 837–846.

[7] X. Liu, J. Cao, S. Tang, and J. Wen, "Wi-Sleep: Contactless sleep monitoring via WiFi signals," in *IEEE Real-Time Systems Symposium 2014*, Dec 2014, pp. 346–355.

[8] O. Kaltiokallio, H. Yiğitler, R. Jäntti, and N. Patwari, "Non-invasive respiration rate monitoring using a single COTS TX-RX pair," in *Proceedings of the 13th International Symposium on Information Processing in Sensor Networks, IPSN-14*, April 2014, pp. 59–69.

[9] N. Patwari, J. Wilson, S. Ananthanarayanan, S. K. Kasera, and D. R. Westenskow, "Monitoring breathing via signal strength in wireless networks," *IEEE Transactions on Mobile Computing*, vol. 13, no. 8, pp. 1774–1786, 2014.

[10] N. Patwari, L. Brewer, Q. Tate, O. Kaltiokallio, and M. Bocca, "Breathfinding: A wireless network that monitors and locates breathing in a home," *IEEE Journal of Selected Topics in Signal Processing*, vol. 8, no. 1, pp. 30–42, Feb 2014.

[11] D. Rife and R. Boorstyn, "Single tone parameter estimation from discrete-time observations," *IEEE Transactions on Information Theory*, vol. 20, no. 5, pp. 591–598, 1974.

[12] H. Yiğitler, O. Kaltiokallio, and R. Jäntti, "Received signal strength models for narrowband radios," in *Positioning and Navigation in Complex Environments*. IGI Global, 2018, pp. 50–87.

[13] H. Yiğitler, "Narrowband radio frequency inference: Physical modeling and measurement processing," Ph.D. dissertation, Aalto University, 2018.

[14] H. Yiğitler, R. Jäntti, O. Kaltiokallio, and N. Patwari, "Detector based radio tomographic imaging," *IEEE Transaction on Mobile Computing*, vol. X, no. X, pp. PP–PP, XX 2017.

[15] O. Kaltiokallio, H. Yiğitler, and R. Jäntti, "A three-state received signal strength model for device-free localization," *IEEE Transaction on Vehicular Technology*, vol. X, no. X, pp. PP–PP, XX 2017.

[16] R. Hostettler, O. Kaltiokallio, H. Yiğitler, S. Särkkä, and R. Jäntti, "RSS-based respiratory rate monitoring using periodic Gaussian processes and Kalman filtering," in *25th European Signal Processing Conference (EUSIPCO)*, Kos, Greece, August 2017.

[17] M. Folke, L. Cernerud, M. Ekström, and B. Hök, "Critical review of non-invasive respiratory monitoring in medical care," *Medical and Biological Engineering and Computing*, vol. 41, no. 4, pp. 377–383, 2003.

[18] C. Li, V. M. Lubecke, O. Boric-Lubecke, and J. Lin, "A review on recent advances in doppler radar sensors for noncontact healthcare monitoring," *IEEE Transactions on Microwave Theory and Techniques*, vol. 61, no. 5, pp. 2046–2060, May 2013.

[19] J. Salmi, O. Luukkonen, and V. Koivunen, "Continuous wave radar based vital sign estimation: Modeling and experiments," in *IEEE Radar Conference (RADAR), 2012*, 2012, pp. 0564–0569.

[20] A. Lazaro, D. Girbau, and R. Villarino, "Analysis of vital signs monitoring using an ir-uwb radar," *Progress In Electromagnetics Research*, vol. 100, pp. 265–284, 2010.

[21] S. Venkatesh, C. R. Anderson, N. V. Rivera, and R. M. Buehrer, "Implementation and analysis of respiration-rate estimation using impulse-based UWB," in *IEEE Military Communications Conference, 2005. MILCOM 2005.* IEEE, 2005, pp. 3314–3320.

[22] F. Adib, Z. Kabelac, D. Katabi, and R. C. Miller, "3D tracking via body radio reflections." in *NSDI*, vol. 14, 2014, pp. 317–329.

[23] H. Abdelnasser, K. A. Harras, and M. Youssef, "UbiBreathe: A ubiquitous non-invasive WiFi-based breathing estimator," in *Pro-*

ceedings of the 16th ACM International Symposium on Mobile Ad Hoc Networking and Computing. ACM, 2015, pp. 277–286.
[24] J. Liu, Y. Wang, Y. Chen, J. Yang, X. Chen, and J. Cheng, "Tracking vital signs during sleep leveraging off-the-shelf WiFi," in *Proceedings of the 16th ACM International Symposium on Mobile Ad Hoc Networking and Computing*. ACM, 2015, pp. 267–276.
[25] H. Wang, D. Zhang, J. Ma, Y. Wang, Y. Wang, D. Wu, T. Gu, and B. Xie, "Human respiration detection with commodity WiFi devices: do user location and body orientation matter?" in *Proceedings of the 2016 ACM International Joint Conference on Pervasive and Ubiquitous Computing*. ACM, 2016, pp. 25–36.
[26] X. Liu, J. Cao, S. Tang, J. Wen, and P. Guo, "Contactless respiration monitoring via off-the-shelf WiFi devices," *IEEE Transactions on Mobile Computing*, vol. 15, no. 10, pp. 2466–2479, 2016.
[27] H. Yiğitler, R. Jäntti, and N. Patwari, "On log-normality of RSSI in narrowband receivers under static conditions," *IEEE Signal Processing Letters*, vol. 24, no. 4, pp. 367–371, April 2017.
[28] P. Hillyard, A. Luong, A. S. Abrar, N. Patwari, K. Sundar, R. Farney, J. Burch, C. Porucznik, and S. H. Pollard, "Experience: Cross-technology radio respiratory monitoring performance study," in *Proceedings of the 24th Annual International Conference on Mobile Computing and Networking*, ser. MobiCom '18. New York, NY, USA: ACM, 2018, pp. 487–496.
[29] A. Luong, A. S. Abrar, T. Schmid, and N. Patwari, "RSS step size: 1 dB is not enough!" in *Proceedings of the 3rd Workshop on Hot Topics in Wireless*. ACM, 2016, pp. 17–21.
[30] T. S. Rappaport, *Wireless Communications: Principles and Practice*, 2nd ed. Prentice Hall, 2002.
[31] A. B. Carlson, P. B. Crilly, and J. Ruttledge, *Communication systems: An introduction to signals and noise in electrical communication*, 4th ed. McGraw-Hill New York, 2002.
[32] M. Abramowitz and I. A. Stegun, *Handbook of mathematical functions: with formulas, graphs, and mathematical tables*. Dover Publications, 1970.
[33] H. Kaneko and J. Horie, "Breathing movements of the chest and abdominal wall in healthy subjects," *Respiratory Care*, vol. 57, no. 9, pp. 1442–1451, 2012.
[34] L. C. Maximon, "The dilogarithm function for complex argument," *Proceedings of the Royal Society of London. Series A: Mathematical, Physical and Engineering Sciences*, vol. 459, no. 2039, pp. 2807–2819, 2003.
[35] S. M. Kay, *Modern Spectral Estimation*. Prentice-Hall, 1988.
[36] Y. Qi, T. P. Minka, and R. W. Picard, "Bayesian spectrum estimation of unevenly sampled nonstationary data," in *IEEE International Conference on Acoustics, Speech, and Signal Processing (ICASSP)*, vol. 2, May 2002, pp. 1473–1476.
[37] S. Särkkä, A. Solin, and J. Hartikainen, "Spatiotemporal learning via infinite-dimensional Bayesian filtering and smoothing: A look at Gaussian process regression through Kalman filtering," *IEEE Signal Processing Magazine*, vol. 30, no. 4, pp. 51–61, July 2013.
[38] C. E. Rasmussen and C. K. I. Williams, *Gaussian Processes for Machine Learning*. MIT Press, 2006.
[39] A. Solin and S. Särkkä, "Explicit link between periodic covariance functions and state space models," in *Proceedings of the 17th International Conference on Artificial Intelligence and Statistics (AISTATS)*, vol. 33, 2014, pp. 904–912.
[40] B. Øksendal, *Stochastic Differential Equations: An Introduction with Applications*, 6th ed. Springer, 2010.
[41] B. G. Quinn, "Estimating frequency by interpolation using Fourier coefficients," *IEEE Transactions on Signal Processing*, vol. 42, no. 5, pp. 1264–1268, 1994.
[42] C. Candan, "A method for fine resolution frequency estimation from three DFT samples." *IEEE Signal Procesing Letters*, vol. 18, no. 6, pp. 351–354, 2011.
[43] H. Yiğitler, R. Jäntti, and R. Virrankoski, "pRoot: An adaptable wireless sensor-actuator hardware platform," in *12th IEEE International Conference on Embedded and Ubiquitous Computing (EUC)*. IEEE, 2014, pp. 281–286.

Hüseyin Yiğitler received the B.Sc. and M.Sc. degrees in electrical and electronics engineering from Middle East Technical University, Ankara, Turkey, in 2004 and 2006 respectively. He received his Ph.D. from Aalto University School of Electrical Engineering in 2018. He holds a Post-Doctoral Researcher position at Aalto University, and taking the chief technology officer role at Biyomod, Ankara, Turkey. His research interests include RF propagation, localization and tracking, signal processing, and design and implementation of embedded (wireless) systems.

Ossi Kaltiokallio received the B.Sc. and M.Sc. degrees in Electrical Engineering from Aalto University, both in 2011, and the D.Sc. (with distinction) degree in Communications Engineering from Aalto University, Finland, in 2017. He has held a Post-Doctoral Fellow position at University of Utah, USA, in 2018. Currently, he holds a Post-Doctoral Researcher position at Aalto University. Dr. Kaltiokallio has received best paper awards from SenseApp (2012) and IPSN (2014). His current research interests include RF propagation, localization and tracking technologies, and statistical signal processing.

Roland Hostettler (S'10-M'14) received the Dipl. Ing. degree in Electrical and Communication Engineering from Bern University of Applied Sciences, Switzerland in 2007, and the M.Sc. degree in Electrical Engineering and Ph.D. degree in Automatic Control from Luleå University of Technology, Sweden in 2009 and 2014, respectively. He has held Post-Doctoral Researcher positions at Luleå University of Technology, Sweden and Aalto University, Finland. Currently, he is a Research Fellow with the Department of Electrical Engineering and Automation, Aalto University, Finland. His research interests include statistical signal processing with applications to target tracking, biomedical engineering, and sensor networks.

Alemayehu Solomon Abrar received B.Sc. degree in Electrical Engineering from Addis Ababa University in 2012. He is currently a Ph.D. candidate at Washington University in St Louis. His current research interests include RF sensing for cyber-physical systems, signal processing, and wireless networking.

Riku Jäntti (M'02 - SM'07) is a Full Professor of Communications Engineering and the head of the department of Communications and Networking at Aalto University School of Electrical Engineering, Finland. He received his M.Sc (with distinction) in Electrical Engineering in 1997 and D.Sc (with distinction) in Automation and Systems Technology in 2001, both from Helsinki University of Technology (TKK). Prior to joining Aalto (formerly known as TKK) in August 2006, he was professor pro tem at the Department of Computer Science, University of Vaasa. Prof. Jäntti is a senior member of IEEE and associate editor of IEEE Transactions on Vehicular Technology. He is also IEEE VTS Distinguished Lecturer (Class 2016). The research interests of Prof. Jäntti include radio resource control and optimization for machine type communications, cloud based radio access networks, quantum communications and RF Inference.

Neal Patwari is a Professor in the School of Engineering and Applied Science at Washington University in St. Louis, where he is appointed in the Dept. of Electrical and Systems Engineering and the Dept. of Computer Science and Engineering. He directs the Sensing and Processing Across Networks (SPAN) Lab, which performs research at the intersection of statistical signal processing and wireless networking, for improving wireless sensor networking and for RF sensing, in which the radio interface is the sensor. Neal has helped to start Xandem Technology, and Sixth Sensing, two companies commercializing RF sensing technologies. His research perspective was shaped by his BS and MS in EE at Virginia Tech, his research work at Motorola Labs in Plantation, Florida, and his Ph.D. in EE at the University of Michigan. He was previously at the University of Utah in Electrical and Computer Engineering from 2006 to 2018. He received the NSF CAREER Award in 2008, the 2009 IEEE Signal Processing Society Best Magazine Paper Award, and the 2011 University of Utah Early Career Teaching Award. He has co-authored papers with best paper awards at IEEE SenseApp 2012 and at the ACM/IEEE IPSN 2014 conference. Neal has served on technical program committees for IPSN, MobiCom, SECON, and SenSys.

Simo Särkkä is an Associate Professor with Aalto University. His research interests are in multi-sensor data processing systems with applications in location sensing, health technology, machine learning, inverse problems, and brain imaging. He has authored or coauthored over 100 peer-reviewed scientific articles and 3 books. He is a Senior Member of IEEE, serving as an Associate Editor of IEEE Signal Processing Letters, and is a member of IEEE Machine Learning for Signal Processing Technical Committee.